Numerical Heat Transfer, Part B, 45: 410–444, 2014

ISSN: 1040-7790 print/1521-0626 online
DOI: 10.1080/10407790.2013.869102

Taylor & Francis
Taylor & Francis Group

A FULLY COUPLED NAVIER-STOKES SOLVER FOR FLUID FLOW AT ALL SPEEDS

M. Darwish and F. Moukalled
Department of Mechanical Engineering, American University of Beirut, Beirut, Lebanon

This article deals with the formulation and testing of a newly developed, fully coupled, pressure-based algorithm for the solution of fluid flow at all speeds. The new algorithm is an extension into compressible flows of a fully coupled algorithm developed by the authors for laminar incompressible flows. The implicit velocity–pressure–density coupling is resolved by deriving a pressure equation following a procedure similar to a segregated SIMPLE algorithm using the Rhie-Chow interpolation technique. The coefficients of the momentum and continuity equations are assembled into one matrix and solved simultaneously, with their convergence accelerated via an algebraic multigrid method. The performance of the coupled solver is assessed by solving a number of two-dimensional problems in the subsonic, transsonic, supersonic, and hypersonic regimes over several grid systems of increasing sizes. For a desired level of convergence, results for each problem are presented in the form of convergence history plots, tabulated values of the maximum number of required iterations, the total CPU time, and the CPU time per control volume.

INTRODUCTION

Despite its wide adoption and success in solving a broad range of flow problems encompassing incompressible [1, 2] and compressible fluid flow at all speeds [3–8], single [9, 10] and multiphase flows [11, 12], laminar [13] and turbulent flows [14–16], free-surface flows [17, 18], and particle-laden flows [19–21], to cite a few, the segregated pressure-based approach [22, 23], built on the SIMPLE family of algorithms [24–26], continues to suffer from a breakdown in convergence rate for large-scale problems. The reason for incompressible flow problems failing to scale linearly with grid size is the weak pressure–velocity coupling that these algorithms use when discretizing the highly coupled Navier-Stokes equations, which in compressible flows extend to the pressure–velocity–density coupling. One way to address this weakness is through the use of the full algebraic storage (FAS) multigrid method [27–29]. Another approach is to ensure that the numerical

Received 24 September 2013; Accepted 7 November 2013.
The financial support provided by the University Research Board of the American University of Beirut is gratefully acknowledged.
Address correspondence to F. Moukalled, Department of Mechanical Engineering, American University of Beirut, P.O. Box 11-0236, Riad El Solh, Beirut, 1107 2020, Lebanon. E-mail: fmukalled@aub.edu.lb

NOMENCLATURE

$a_C^{uu}, a_F^{uv}, \ldots$	coefficients in the discretized equations
b_P^u	source term in the discretized equations
B	source term in the momentum equation
C	main grid point
$\mathbf{d}_{CF}$	vector joining the grid points C and F
D	operator used in the pressure equation
E	component of the surface vector in the direction of $\mathbf{d}_{CF}$
F	refers to neighbor of the C grid point
g	geometric interpolation factor
i, **j**	unit vectors in the x and y directions, respectively
$\dot{m}_f$	mass flow rate at control-volume face f
p	pressure
P	main grid point
Q	general source term
RMS	root-mean-square residuals
S	surface vector
t	time
T	component of the surface vector to **S**
u, v	velocity components in x and y directions, respectively
v	velocity vector
μ	dynamic viscosity
ρ	fluid density
τ	deviatoric stress tensor

Subscripts

C	refers to main grid point
f	refers to control-volume face
F	refers to the F grid point
nb	refers to values at the faces obtained by interpolation between C and its neighbors
NB	refers to the neighbors of the C grid point

Superscripts

p	refers to pressure
u	refers to the u-velocity component
v	refers to the v-velocity component
$\circ$	refers to value at the previous time step
$*$	refers to value at the previous iteration
$**$	refers to value at the current iteration
—	refers to an interpolated value

discretization reflects the strong coupling that exists in the Navier-Stokes equations. In this case all equations are solved simultaneously in a coupled fashion as opposed to a segregated approach. As described in [30], such an approach is actually used in density-based methods [31, 32], where the Navier-Stokes and energy equations are solved simultaneously as one system of equations. It is worth mentioning that the Computational fluid dynamics (CFD) group at Imperial College, originator of the SIMPLE algorithm, had initially developed a coupled pressure-based solver [33] and not a segregated solver. However, their coupled algorithm, known as SIVA, was overshadowed by the SIMPLE algorithm, which combined low memory requirement with coding simplicity, two substantial advantages given the state of computer technology at that time. Recent advances in computer architecture renewed interest in coupled algorithms and led to the development of a number of new approaches [34–37]. A coupled algorithm for incompressible flows has been successfully implemented by the authors [38, 39], showing near-linear scalability for grids in the range 10,000 to 300,000 elements. The current work extends the coupled algorithm to compressible flow situations. This extension requires mass conservation to be expressed not only by a change in pressure, but also by a change in density. Therefore the algorithm must express this relationship in its numerics to be able to resolve supersonic, transsonic, or even subsonic flows at a Mach number greater than about 0.3.

The compressible pressure-based coupled algorithm is presented next by first detailing the finite-volume discretization of its coupled equations. Then a set of

problems is presented that illustrate the convergence and computational cost of the coupled solver. The performance is assessed by solving a number of two-dimensional problems over several grid systems of increasing size and noting the solver performance to convergence in terms of number of iterations, CPU time, and computational cost per control volume.

DISCRETIZATION OF INTERNAL ELEMENTS

In the coupled approach the momentum and mass conservation equations are solved simultaneously. The mass conservation equation is not used in its original form; rather, it is transformed into a pressure equation that is coupled to the velocity field of the momentum conservation equation. Thus the velocity and pressure fields are calculated simultaneously based on guessed or estimated velocity and pressure fields to obtain pressure and velocity fields that satisfy both the momentum conservation and mass conservation. This technique guarantees momentum and mass conservation at any iteration. The discretization process proceeds as follows: The solution domain is first discretized by subdividing it into a number of control volumes with each one associated with a main grid point C (Figure 1) placed at its centroid. Then the conservation equations are discretized using a two-step procedure as described next for the various equations.

Momentum Equation

The vector form of the momentum equation can be written as

$$\frac{\partial (\rho \mathbf{v})}{\partial t} + \nabla \cdot (\rho \mathbf{v}\mathbf{v}) = -\nabla p + \nabla \cdot \tau + \mathbf{B} \tag{1}$$

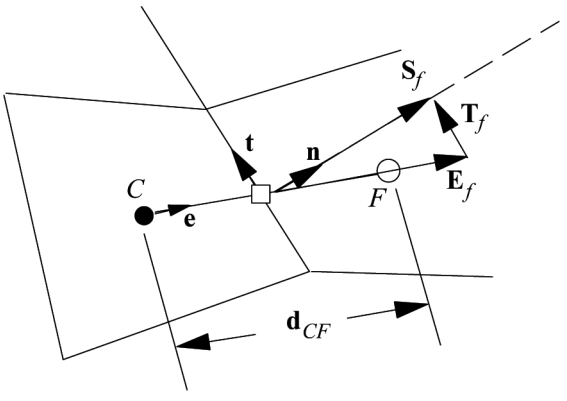

Figure 1. A schematic of a control volume C, its neighbor control volume F, and related geometric quantities.

The discretization process starts by first integrating Eq. (1) over the control volume shown in Figure 1, to yield

$$\iint_{\Omega} \frac{\partial(\rho \mathbf{v})}{\partial t} d\Omega + \iint_{\Omega} \nabla \cdot (\rho \mathbf{v}\mathbf{v})\, d\Omega = -\iint_{\Omega} \nabla p\, d\Omega + \iint_{\Omega} \nabla \cdot \tau\, d\Omega + \iint_{\Omega} \mathbf{B}\, d\Omega \quad (2)$$

where Ω is the volume of the control volume whose surface is denoted by $\partial\Omega$. The volume integrals are then transformed into surface integral using the divergence theorem. This results in

$$\iint_{\Omega} \frac{\partial(\rho \mathbf{v})}{\partial t} d\Omega + \oint_{\partial\Omega} (\rho \mathbf{v}\mathbf{v}) \cdot d\mathbf{S} = -\oint_{\partial\Omega} p\, d\mathbf{S} + \oint_{\partial\Omega} \tau \cdot d\mathbf{S} + \iint_{\Omega} \mathbf{B} d\Omega \quad (3)$$

Adopting an implicit Euler integration scheme for the transient term and evaluating surface and volume integrals using a second-order interpolation profile (trapezoidal rule), Eq. (3) is transformed to

$$\frac{(\rho \mathbf{v}) - (\rho \mathbf{v})^{\circ}}{\partial t} \Omega_C + \sum_{f=\mathrm{nb}(C)} (\rho \mathbf{v}\mathbf{v} - \tau)_f \cdot \mathbf{S}_f + \sum_{f=\mathrm{nb}(C)} p_f \mathbf{S}_f = \mathbf{B}_C \Omega_C \quad (4)$$

All terms appearing in Eq. (4) are evaluated at time t except for the term $(\rho \mathbf{v})^{\circ}$, which is evaluated at time $t - \Delta t$. Finally, the equation is transformed into an algebraic equation by expressing the variation in the dependent variable and its derivatives in terms of the grid-point values. The resulting equation links the value of the dependent variable at the control-volume center to the neighboring dependent-variable values and is given by

$$a_C^{\mathbf{vv}} \mathbf{v}_C + \sum_{F=\mathrm{NB}(C)} a_F^{\mathbf{vv}} \mathbf{v}_F + a_C^{\mathbf{v}p} p_C + \sum_{F=\mathrm{NB}(C)} a_F^{\mathbf{v}p} p_F = \mathbf{b}_C^{\mathbf{v}} \quad (5)$$

where

$$\begin{cases} a_C^{\mathbf{vv}} = \frac{\rho \Omega_P}{\Delta t} + \sum_{f=\mathrm{nb}(C)} \left(\mu \frac{\|\mathbf{E}_f\|}{\|\mathbf{d}_{CF}\|} + \|\dot{m}_f, 0\| \right) & a_F^{\mathbf{vv}} = -\mu \frac{\|\mathbf{E}_f\|}{\|\mathbf{d}_{CF}\|} - \|-\dot{m}_f, 0\| \\ a_C^{\mathbf{v}p} = g_C \mathbf{S}_f \quad a_F^{\mathbf{v}p} = g_F \mathbf{S}_f & \mathbf{b}_C^{\mathbf{v}} = \mathbf{B}_C \Omega_C + \frac{(\rho \mathbf{v})^{\circ}}{\Delta t} \Omega_C - \sum_{f=\mathrm{nb}(C)} \left(\mu \tau \cdot \mathbf{T}_f + \|\dot{m}_f, 0\| \right) \end{cases} \quad (6)$$

The vectors $\mathbf{d}_{CF}$, $\mathbf{E}_f$, and $\mathbf{T}_f$ are displayed in Figure 1. When the interest is in a steady-state solution, the transient contribution to the $\mathbf{b}_C^{\mathbf{v}}$ term is modified into a false transient term and instead of the old value the previous value of the computed field is used as

$$\mathbf{b}_C^{\mathbf{v}} = \mathbf{B}_C \Omega_C + \frac{(\rho \mathbf{v})^{*}}{\Delta t} \Omega_C - \sum_{f=nb(C)} \left(\mu \tau \cdot \mathbf{T}_f + \|\dot{m}_f, 0\| \right) \quad (7)$$

Continuity Equation

The semidiscrete form of the continuity equation can be written as

$$\frac{\rho-\rho^{\circ}}{\Delta t}\Omega_C+\sum_{f=\mathrm{nb}(C)}\dot{m}_f=0 \tag{8}$$

In this equation the pressure and density fields are related by the ideal gas relation as

$$\rho=\left(\frac{1}{RT}\right)p=C_\rho p \tag{9}$$

At any point the density, velocity, and pressure fields can be defined as ρ^*, $\mathbf{v}^*$, and p^*, with these fields not completely satisfying the momentum and mass conservation equations. The aim is to derive updated fields ρ^{**}, $\mathbf{v}^{**}$, and p^{**} that better satisfy these conservation equations. Using the updated fields, the continuity equation is given by

$$\frac{\rho_C^{**}-\rho_C^{\circ}}{\partial t}\Omega_C+\sum_{f=\mathrm{nb}(C)}\rho_f^{**}\mathbf{v}_f^{**}\cdot\mathbf{S}_f=0 \tag{10}$$

Applying a Newtonian linearization, the change in $\rho_f\mathbf{v}_f$ with iterations (n) can be written as

$$\begin{aligned}\frac{d\left(\rho_f\mathbf{v}_f\right)^*}{dn}&=\frac{\left(\rho_f\mathbf{v}_f\right)^{**}-\left(\rho_f\mathbf{v}_f\right)^*}{(n+1)-n}=\rho_f^*\frac{d\mathbf{v}_f^*}{dn}+\mathbf{v}_f^*\frac{d\rho_f^*}{dn}\rho_f^{**}\mathbf{v}_f^{**}-\rho_f^*\mathbf{v}_f^*\\&=\rho_f^*\left(\mathbf{v}_f^{**}-\mathbf{v}_f^*\right)+\mathbf{v}_f^*\left(\rho_f^{**}-\rho_f^*\right)\Rightarrow\rho_f^{**}\mathbf{v}_f^{**}=\rho_f^*\mathbf{v}_f^{**}+\rho_f^{**}\mathbf{v}_f^*-\rho_f^*\mathbf{v}_f^*\end{aligned} \tag{11}$$

Substituting the value of $\rho_f^{**}\mathbf{v}_f^{**}$ from Eq. (11) into Eq. (10), the continuity equation becomes

$$\frac{\rho_C^{**}-\rho_C^{\circ}}{\Delta t}\Omega_C+\sum_{f=\mathrm{nb}(C)}\left(\rho_f^*\mathbf{v}_f^{**}\cdot\mathbf{S}_f+\overbrace{\rho_f^{**}\mathbf{v}_f^*\cdot\mathbf{S}_f-\rho_f^*\mathbf{v}_f^*\cdot\mathbf{S}_f}^{\text{compressible}}\right)=0 \tag{12}$$

where the terms labeled "compressible" in Eq. (12), and others presented later, are additional terms arising due to compressibility effects. Using the ideal gas relation, Eq. (12) is changed to

$$\frac{C_\rho^*p_C^{**}-\rho_C^{\circ}}{\Delta t}\Omega_C+\sum_{f=\mathrm{nb}(C)}\left(\rho_f^*\mathbf{v}_f^{**}\cdot\mathbf{S}_f+\overbrace{C_\rho^*\frac{\dot{m}_f^*}{\rho_f^*}p_f^{**}-\dot{m}_f^*}^{\text{compressible}}\right)=0 \tag{13}$$

The discretization of the continuity equation needs further treatment in order to derive the pressure equation. This is because, unlike the momentum equation, which is a primitive equation for velocity, continuity acts as a constraint on the pressure

field. For a collocated grid system, coupling of the pressure and velocity fields is ensured by computing the velocity at the control-volume faces using the Rhie-Chow interpolation [3], according to which the interface velocity is given by

$$\mathbf{v}_f = \overline{\mathbf{v}_f} - \overline{\mathbf{D}_f}\left(\nabla p_f - \overline{\nabla p_f}\right) \tag{14}$$

where the averaged quantity $\overline{\square}_f$ is computed using linear interpolation as

$$\overline{\mathbf{v}_f} = g_C\mathbf{v}_C + g_F\mathbf{v}_F \quad \overline{\nabla p_f} = g_C\nabla p_C + g_F\nabla p_F \quad \overline{\mathbf{D}_f} = g_C\mathbf{D}_C + g_F\mathbf{D}_F \quad g_C + g_F = 1 \tag{15}$$

Substituting Eq. (14) into Eq. (13), the continuity equation after manipulation becomes

$$\overbrace{\frac{C_\rho^*\Omega_C}{\Delta t}p_C^{**} + \sum_{f=nb(C)}\left(\frac{C_\rho^*}{\rho_f^*}\dot{m}_f^* p_f^{**}\right)}^{\text{compressible}} + \sum_{f=\text{nb}(C)}\left[\rho_f^*\overline{\mathbf{v}_f^{**}} - \rho_f^*\overline{D}_f\nabla p_f^{**}\right]\cdot\mathbf{S}_f$$
$$= \overbrace{\frac{\Omega_C}{\Delta t}\rho_C^\circ + \sum_{f=\text{nb}(C)}\dot{m}_f^*}^{\text{compressible}} - \sum_{f=\text{nb}(C)}\left(\rho_f^*\overline{D}_f\overline{\nabla p_f^*}\cdot\mathbf{S}_f\right) \tag{16}$$

Combining this pressure equation with the momentum equation [Eq. (5)] yields the following system of equation with $\mathbf{v}^{**}$ and p^{**} as variables:

$$\begin{bmatrix} a_C^{\mathbf{vv}} & a_C^{\mathbf{v}p} \\ a_C^{p\mathbf{v}} & a_C^{pp} \end{bmatrix}\begin{bmatrix} \mathbf{v}_C^{**} \\ p_C^{**} \end{bmatrix} + \sum_{F=\text{NB}(C)}\begin{bmatrix} a_F^{\mathbf{vv}} & a_F^{\mathbf{v}p} \\ a_F^{p\mathbf{v}} & a_F^{pp} \end{bmatrix}\begin{bmatrix} \mathbf{v}_F^{**} \\ p_F^{**} \end{bmatrix} = \begin{bmatrix} \mathbf{b}_C^{\mathbf{v}} \\ b_C^p \end{bmatrix} \tag{17}$$

For a two-dimensional flow problem this is written as

$$\begin{bmatrix} a_C^{uu} & a_C^{uv} & a_C^{up} \\ a_C^{vu} & a_C^{vv} & a_C^{vp} \\ a_C^{pu} & a_C^{pv} & a_C^{pp} \end{bmatrix}\begin{bmatrix} u_C^{**} \\ v_C^{**} \\ p_C^{**} \end{bmatrix} + \sum_{F=\text{NB}(C)}\begin{bmatrix} a_F^{uu} & a_F^{uv} & a_F^{up} \\ a_F^{vu} & a_F^{vv} & a_F^{vp} \\ a_F^{pu} & a_F^{pv} & a_F^{pp} \end{bmatrix}\begin{bmatrix} u_F^{**} \\ v_F^{**} \\ p_F^{**} \end{bmatrix} = \begin{bmatrix} b_C^u \\ b_C^v \\ b_C^p \end{bmatrix} \tag{18}$$

where the coefficients are given as follows.

Coefficients for the u-velocity equation:

$$a_C^{uu} = \frac{\rho_C^*\Omega_C}{\Delta t} + \sum_{f=\text{nb}(C)}\left(\mu_f\frac{\|\mathbf{E}_f\|}{\|\mathbf{d}_{CF}\|} + \|\dot{m}_f^*, 0\|\right) \quad a_F^{uu} = -\mu_f\frac{\|\mathbf{E}_f\|}{\|\mathbf{d}_{CF}\|} - \|-\dot{m}_f^*, 0\|$$
$$a_C^{uv} = 0 \quad a_F^{uv} = 0 \quad a_C^{up} = \sum_{f=nb(C)} g_{fC}\mathbf{S}_f\cdot\mathbf{i} \quad a_F^{up} = g_{fF}\mathbf{S}_f\cdot\mathbf{i}$$
$$b_C^u = \frac{\rho_C^* u_C^\circ}{\Delta t}\Omega_C + \mathbf{B}_C\cdot\mathbf{i}\Omega_C + \sum_{f=\text{nb}(C)}\left(\mu_f\nabla u_f^*\cdot\mathbf{T}_f\right) + \sum_{f=\text{nb}(C)}\left[\frac{1}{3}\mu_f\left(\nabla\cdot\mathbf{v}_f^*\right)\mathbf{i}\cdot\mathbf{S}_f\right] \tag{19}$$

Coefficients for the v-velocity equation:

$$a_C^{vv} = \frac{\rho_C^* \Omega_C}{\Delta t} + \sum_{f=\mathrm{nb}(C)} \left(\mu_f \frac{\|\mathbf{E}_f\|}{\|\mathbf{d}_{CF}\|} + \|\dot{m}_f^*, 0\| \right) \quad a_F^{vv} = -\mu_f \frac{\|\mathbf{E}_f\|}{\|\mathbf{d}_{CF}\|} - \|-\dot{m}_f^*, 0\|$$

$$a_C^{vu} = 0 \quad a_F^{vu} = 0 \quad a_C^{vp} = \sum_{f=\mathrm{nb}(C)} g_{fC} \mathbf{S}_f \cdot \mathbf{j} \quad a_F^{vp} = g_{fF} \left(\mathbf{S}_f \cdot \mathbf{j} \right)$$

$$b_C^v = \frac{\rho_C^* v_f^\circ}{\Delta t} \Omega_C + \left(\mathbf{B}_C \cdot \mathbf{j} \right) \Omega_C + \sum_{f=\mathrm{nb}(C)} \left(\mu_f \nabla v_f^* \cdot \mathbf{T}_f \right) + \sum_{f=\mathrm{nb}(C)} \left[\frac{1}{3} \mu_f \left(\nabla \cdot \mathbf{v}_f^* \right) \mathbf{j} \cdot \mathbf{S}_f \right] \quad (20)$$

Coefficients for the pressure equation:

$$a_C^{pp} = \frac{\Omega_C}{RT_C^* \Delta t} + \sum_{f=\mathrm{nb}(C)} \left(\overline{D_f} \frac{\|\mathbf{E}_f\|}{\|\mathbf{d}_{CF}\|} + \left\| \frac{\dot{m}_f^*}{\rho_f^*} C_\rho, 0 \right\| \right) \quad a_F^{pp} = -\overline{D_f} \frac{\|\mathbf{E}_f\|}{\|\mathbf{d}_{CF}\|} - \left\| -\frac{\dot{m}_f^*}{\rho_f^*} C_\rho, 0 \right\|$$

$$a_C^{pu} = \sum_{f=\mathrm{nb}(C)} g_{fC} \mathbf{S}_f \cdot \mathbf{i} \quad a_F^{pu} = g_{fF} \left(\mathbf{S}_f \cdot \mathbf{i} \right) \quad a_C^{pv} = \sum_{f=\mathrm{nb}(C)} g_{fC} \mathbf{S}_f \cdot \mathbf{j} \quad a_F^{pv} = g_{fF} \left(\mathbf{S}_f \cdot \mathbf{j} \right)$$

$$b_C^p = -\sum_{f=\mathrm{nb}(C)} \dot{m}_f^* + \sum_{f=\mathrm{nb}(C)} \left(\overline{D_f} \nabla p_f^* \cdot \mathbf{T}_f \right) \quad (21)$$

DISCRETIZATION OF BOUNDARY ELEMENTS

A boundary element has at least a boundary face where boundary conditions are applied. The treatment of these boundary conditions is critical to the accuracy and robustness of any numerical scheme. For coupled algorithms it greatly affects the convergence history, since at these boundaries additional coupling needs to be taken into account. For example, the a^{uv} and a^{vu} coefficients are nonzero at wall boundaries; also, the a^{pu} and a^{pv} coefficients are greatly affected by the type of boundary condition at inlets and outlets. The general discretization of the continuity and momentum equations along a boundary element is presented next. The full discretization of the different types of boundary conditions will be the subject of a future article.

Momentum Equation

The semidiscretized form of the momentum equation can be expressed as

$$\underbrace{\frac{(\rho \mathbf{v})_C - (\rho \mathbf{v})_C^\circ}{\Delta t} \Omega_P}_{\text{element discretization}} + \underbrace{\sum_{f=\mathrm{nb}(C)} \left(\dot{m}_f \mathbf{v}_f \right)}_{\text{face discretization}} = \underbrace{-\sum_{f=\mathrm{nb}(C)} \left(P_f \mathbf{S}_f \right)}_{\text{face discretization}} + \underbrace{\sum_{f=\mathrm{nb}(C)} \left(\tau_f \cdot \mathbf{S}_f \right)}_{\text{face discretization}} + \underbrace{\mathbf{B}}_{\text{element discretization}} \quad (22)$$

where the discretization type of the various terms is explicitly stated. Terms that are evaluated at the control-volume faces should be modified along a boundary face in accordance with the type of boundary condition used. Therefore, for boundary

elements, the terms evaluated at the control-volume faces are written as

$$\begin{cases} \underbrace{\sum_{f=\mathrm{nb}(C)} (\dot{m}_f \mathbf{v}_f)}_{\text{face discretization}} = \sum_{f=\text{interior nb}(C)} (\dot{m}_f \mathbf{v}_f) + \underbrace{\dot{m}_b \mathbf{v}_b}_{\text{boundary term}} \\ \underbrace{\sum_{f=\mathrm{nb}(C)} (\tau_f \cdot \mathbf{S}_f)}_{\text{face discretization}} = \sum_{f=\text{interior nb}(C)} (\tau_f \cdot \mathbf{S}_f) + \underbrace{\tau_b \cdot \mathbf{S}_b}_{\text{boundary term}} \\ \qquad = \sum_{f=\text{interior nb}(C)} (\tau_f \cdot \mathbf{S}_f) + \underbrace{\mathbf{F}_b}_{\text{boundary term}} \\ \underbrace{\sum_{f=nb(C)} (P_f \mathbf{S}_f)}_{\text{face discretization}} = \sum_{f=\text{interior nb}(C)} (P_f \mathbf{S}_f) + \underbrace{P_b \mathbf{S}_b}_{\text{boundary term}} \end{cases} \tag{23}$$

where subscript b refers to value at the boundary.

Continuity Equation

The semidiscretized form of the continuity equation can be stated as

$$\underbrace{\frac{\rho_C - \rho_C^\circ}{\Delta t} \Omega_C}_{\text{element discretization}} + \underbrace{\sum_{f=\mathrm{nb}(C)} \dot{m}_f}_{\text{face discretization}} = 0 \tag{24}$$

Similar to the momentum equation, for boundary elements the term evaluated at the control-volume face is written as

$$\underbrace{\sum_{f=\mathrm{nb}(C)} \dot{m}_f}_{\text{face discretization}} = \sum_{f=\text{interior nb}(C)} (\dot{m}_f) + \underbrace{\dot{m}_b}_{\text{boundary term}} = \sum_{f=\text{interior nb}(C)} (\rho_f \mathbf{v}_f \cdot \mathbf{S}_f) + \underbrace{\rho_b \mathbf{v}_b \cdot \mathbf{S}_b}_{\text{boundary term}} \tag{25}$$

Note that for the case of compressible flow a Newtonian linearization is applied to yield

$$\begin{aligned} \underbrace{\sum_{f=nb(C)} (\rho_f^{**} \mathbf{v}_f^{**} \cdot \mathbf{S}_f)}_{\text{face discretization}} &= \sum_{f=\text{interior nb}(C)} (\rho_f^{*} \mathbf{v}_f^{**} \cdot \mathbf{S}_f) + \sum_{f=\text{interior nb}(C)} (\rho_f^{**} \mathbf{v}_f^{*} \cdot \mathbf{S}_f) \\ &\quad - \sum_{f=\text{interior nb}(C)} (\rho_f^{*} \mathbf{v}_f^{*} \cdot \mathbf{S}_f) \\ &\quad + \underbrace{\rho_b^{*} \mathbf{v}_b^{**} \cdot \mathbf{S}_b + \rho_b^{**} \mathbf{v}_b^{*} \cdot \mathbf{S}_b - \rho_b^{*} \mathbf{v}_b^{*} \cdot \mathbf{S}_b}_{\text{boundary term}} \end{aligned} \tag{26}$$

with the implementation taking the form

$$\underbrace{\sum_{f=\mathrm{nb}(C)} \left(\rho_f^{**}\mathbf{v}_f^{**}\cdot\mathbf{S}_f\right)}_{\text{face discretization}} = \sum_{f=\text{interior nb}(C)} \left(\rho_f^{*}\mathbf{v}_f^{**}\cdot\mathbf{S}_f\right)$$
$$+ \overbrace{\sum_{f=\text{interior nb}(C)} \left(\frac{\dot{m}_f^*}{\rho_f^*}\right)\rho_f^{**} - \sum_{f=\text{interior nb}(C)} \dot{m}_f^*}^{\text{compressible}} + \underbrace{\rho_b^*\mathbf{v}_b^{**}\cdot\mathbf{S}_b + \overbrace{\left(\frac{\dot{m}_b^*}{\rho_b^*}\right)\rho_b^{**} - \dot{m}_b^*}^{\text{compressible}}}_{\text{boundary term}} \quad (27)$$

THE RHIE-CHOW INTERPOLATION

As mentioned earlier, the interface velocity is computed using the Rhie-Chow interpolation technique [3] such that the mass flow rate is calculated as

$$\dot{m}_f^{**} = \rho_f^*\cdot\mathbf{S}_f + \overbrace{\left(\frac{\dot{m}_f^*}{\rho_f^*}\right)\rho_f^{**} - \dot{m}_f^*}^{\text{compressible}} = \rho_f^*\left(\boxed{\overline{\mathbf{v}_\mathbf{f}^{**}} - \overline{\mathbf{D}}\left(\nabla p_f^{**} - \overline{\nabla p_f^{**}}\right)}\right)\cdot\mathbf{S}_f$$
$$+ \overbrace{\left(\frac{\dot{m}_f^*}{\rho_f^*}\right)\rho_f^{**} - \dot{m}_f^*}^{\text{compressible}} \quad (28)$$

At boundary faces the treatment of the velocity depends on whether the mass flow rate or the pressure is the specified variable. Generally three types of boundary conditions are distinguished. The first type can be designated by "specified mass flow rate" (e.g., walls, velocity specified at inlets for incompressible flow). For this category, $\dot{m}_b$ has a specified value and no modification to the pressure equation is needed. This yields a Von Newman–like boundary condition for the pressure, with the mass flux ($\dot{m}_b$) being specified. The pressure, however, has to be computed at the boundary from the interior field.

The second type is "pressure specified," where p_b has a specified value. For this boundary condition type, p_b is written in terms of the velocity vector and pressure gradient of the nearest element, yielding a Dirichlet-like condition that should be enforced on the pressure equation.

In the third type, an implicit relation exists between the pressure and the mass flow rate, as in a specified total pressure boundary condition. In this case, an explicit equation is extracted from the implicit relation and substituted into the pressure equation, yielding a hybrid boundary condition.

The type of pressure boundary condition also affects the treatment of the pressure gradient term in the momentum equations. One more detail of interest is the expression for the Rhie-Chow interpolation at the boundary faces. For boundary faces the averaging in the Rhie-Chow interpolation is written in terms of the boundary cell only as

$$\overline{\square}_b = \square_C \quad (29)$$

Thus

$$\overline{\mathbf{v}_b^*} = \mathbf{v}_C^* \quad \overline{\nabla p_b^{(n)}} = \nabla p_C^{(n)} \quad \overline{\mathbf{D}_b} = \mathbf{D}_C \ \ldots \tag{30}$$

and the Rhie-Chow interpolation at the boundary becomes

$$\underset{\text{boundary face}}{\mathbf{v}_b^{**}} = \underbrace{\mathbf{v}_C^{**} - \mathbf{D}_C\left(\nabla p_b^{**} - \nabla p_C^{**}\right)}_{\text{boundary Rhie-Chow}} \tag{31}$$

with the mass flow rate computed as

$$\begin{aligned}
\dot{m}_b^{**} &= \rho_b^* \left(\boxed{\mathbf{v}_{\mathbf{c}}^{**} - \mathbf{D}_c\left(\nabla p_b^{**} - \nabla p_c^*\right)} \right) \cdot \mathbf{S}_b + \overbrace{\left(\frac{\dot{m}_b^*}{\rho_b^*}\right)\rho_b^{**} - \dot{m}_b^*}^{\text{compressible}} \\
&= \rho_b^* \mathbf{v}_C^{**} \cdot \mathbf{S}_b - D_C \frac{\|\mathbf{E}_b\|}{\|\mathbf{d}_{Cb}\|}\left(p_b^{**} - p_C^{**}\right) - \left(\mathbf{D}_C \nabla p_b^{**} \cdot \mathbf{T}_b - \mathbf{D}_C \nabla p_C^{**} \cdot \mathbf{S}_b\right) \\
&\quad + \overbrace{\left(\frac{\dot{m}_b^*}{\rho_b^*}\right)\rho_b^{**} - \dot{m}_b^*}^{\text{compressible}}
\end{aligned} \tag{32}$$

RESULTS AND DISCUSSION

The validity and performance of the coupled algorithm is assessed in this section by presenting solutions to the following steady inviscid two-dimensional test cases: (1) flow over a NACA0012 airfoil; (2) flow over a circular arc bump; (3) supersonic flow over an obstacle; (4) supersonic flow over a circular cylinder; (5) hypersonic flow over a wedge; (6) and flow in a converging-diverging nozzle. Each problem is solved, starting from the same initial guess, over several grid systems of increasing density using triangular and quadrilateral elements. For all problems, computations were terminated when the normalized root-mean-square (RMS) residuals, defined as

$$\begin{aligned}
&RMS = \frac{1}{N}\sqrt{\sum_{i=1}^{N}\left(\frac{a_C^{\varphi}\varphi_C + \sum_{F=\mathrm{NB}(C)} a_F^{\varphi}\varphi_F - b_C^{\varphi}}{a_C^{\varphi}\varphi_{\text{scale}}}\right)^2} \quad N = \text{number of elements} \\
&\varphi_{scale} = \max\left(\varphi_{C,\max} - \varphi_{C,\min}, \varphi_{C,\max}\right) \quad \varphi_{C,\max} = \max_{i=1}^{N}\left(\varphi_C\right) \quad \varphi_{C,\min} = \min_{i=1}^{N}\left(\varphi_C\right)
\end{aligned} \tag{33}$$

over the domain and for all dependent variables fell below 10^{-5}. All computations were performed on a MacPro computer with a 2.8-GHz Intel Xeon processor.

Problem 1: Flow over a NACA0012 Airfoil

The first test case considered is for the steady flow around a NACA 0012 airfoil, which is a standard test case used by several researchers to validate CFD codes [28, 40–44]. For every grid system considered, two flow conditions are simulated. In the first, the flow approaching the airfoil, shown schematically in

Figure 2*a*, is at a Mach number of 0.63 and an angle of attack $\alpha = 2°$. Under these conditions the flow over the airfoil is fully subsonic. In the second configuration, the free-stream Mach number is set at 0.85 and α at 1° resulting in a transsonic flow with shock waves forming on the upper and lower sides of the airfoil. For each flow condition, the problem is solved using quadrilateral elements over three grid systems with sizes of 34,000, 136,000, and 406,000 control volumes. Solutions are also generated using triangular elements over three grid networks with sizes of 43,000, 120,000, and 370,000 control volumes. An illustrated grid generated is depicted in Figure 2*b*.

For subsonic flow conditions isobars are presented in Figure 2*c*, while convergence history plots of the continuity, momentum, and energy equations for the various grid systems and element types are displayed in Figure 3. The reduction of residuals with number of iterations for quadrilateral elements is depicted in Figures 3*a*–3*c*, while those for triangular elements are presented in Figures 3*d*–3*f*. As shown, the convergence paths for all cases are similar.

A summary of the number of iterations, CPU time, and CPU time per control volume are presented for all grid sizes in Table 1*a*. As depicted, the number of iterations varies between 24, for a grid size of 34,000 quadrilateral control volumes, and 79, for a grid size of 370,000 triangular control volumes. The CPU time increases from 233 s for the case of 34,000 quadrilateral control volumes to 16,289 s for the case of 370,000 triangular control volumes. A more indicative performance parameter is the CPU per control volume, which for a quadrilateral element increases from 6.85×10^{-3} s to 31.46×10^{-3}s when the grid size increases from 34,000 to 406,000 control volumes. This represents around a 359.27% increase in the solution cost per control volume for a 1,094.12% increase in the mesh size. For a triangular element, the CPU per control volume increases from 16.26×10^{-3}s to 44.02×10^{-3}s as the grid size increases from 43,000 to 370,000 control volumes.

Results for the transsonic flow case are presented in Figures 4 and 5. Figure 4*a* depicts isobars around the airfoil, with the shocks developing on the upper and lower surfaces of the airfoil clearly seen. Moreover Figure 4*b* presents a comparison of the variation of the pressure coefficient on the upper and lower sides of the airfoil between values generated using the coupled solver and similar ones reported by Favini [40]. As shown, C_p results are on top of each other, indicating a correct implementation of the newly developed coupled method. Again, the convergence history plots over the various grid systems and element types are displayed in Figure 5. The reduction of residuals with number of iterations for quadrilateral elements is depicted in Figures 5*a*–5*c*, while those for triangular elements are presented in Figures 5*d*–5*f*. As shown, the convergence paths for all cases are similar.

A summary of the number of iterations, the CPU time, and CPU time per control volume are presented for all grid sizes in Table 1*b*. As depicted, the number of iterations in this case is greater than the number of iterations required in the subsonic case due to the more complex flow to be resolved. The number of iterations varies between 117, for a grid with size of 34,000 quadrilateral control volumes, and 733, for a grid with size of 370,000 triangular control volumes. The CPU time increases from 1,288 s for the case of 34,000 quadrilateral control volumes to 150,690 s for the case of 370,000 triangular control volumes. At the same time, the

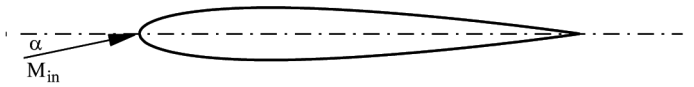

(a)

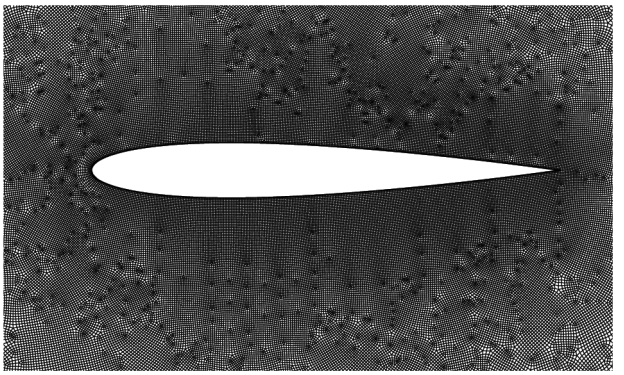

(b)

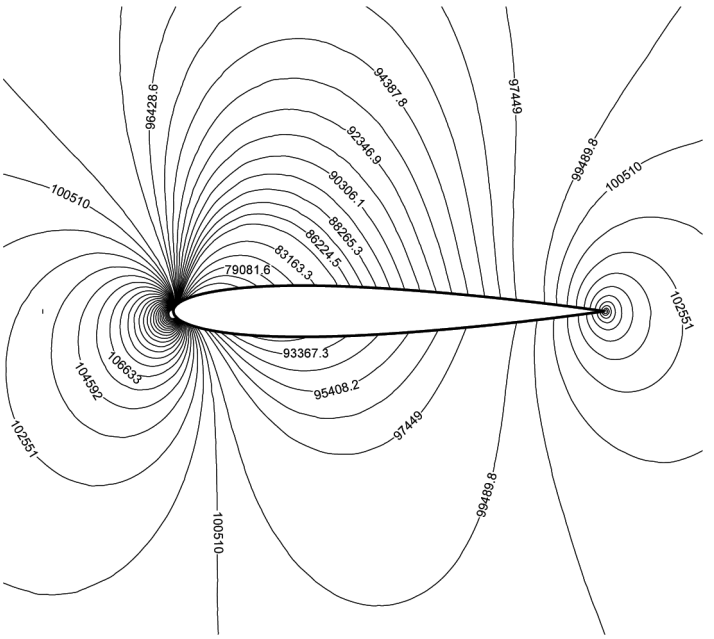

(c)

Figure 2. (*a*) The physical situation for the flow around a NACA 0012 airfoil; (*b*) an illustrative grid in the region close to the airfoil; and (*c*) isobars for subsonic flow over a NACA 0012 airfoil ($M_\infty = 0.63$, $\alpha = 2°$).

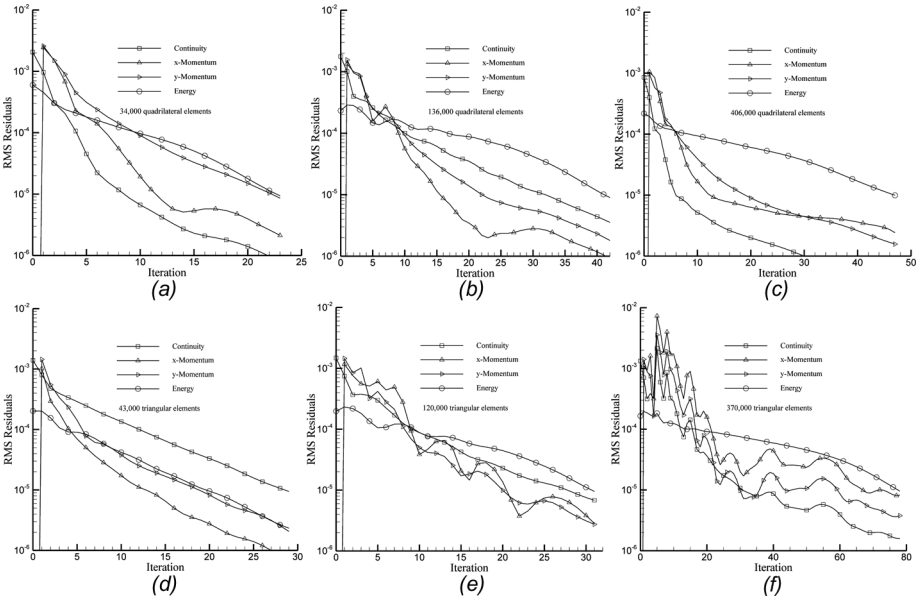

Figure 3. Convergence history for subsonic flow over a NACA0012 airfoil ($M_\infty = 0.63, \alpha = 2°$).

CPU per control volume for quadrilateral elements increases from 37.88×10^{-3} s to 254.46×10^{-3} s when the grid size increases from 34,000 to 406,000 control volumes, while for triangular elements it increases from 9.14×10^{-3} s to 407.27×10^{-3} s as the grid size increases from 43,000 to 370,000 control volumes. Nevertheless, it was possible to obtain solutions with all grid systems used.

Problem 2: Flow over a Circular Arc Bump

The physical situation shown schematically in Figure 6*a* represents a channel of width equal to the length of the circular arc bump and of total length equal to three lengths of the bump [10, 40, 45]. Results are presented for flow in the subsonic, transonic, and supersonic regimes. For subsonic and transsonic calculations, the thickness-to-chord ratio is 10%, and for supersonic flow calculations it is 4%. When available, predictions are compared with published data.

Case 1: Subsonic flow over a circular arc bump. With an inlet Mach number of 0.5, the inviscid flow in the channel is fully subsonic and almost symmetric across the middle of the bump. At the inlet, the flow is assumed to have uniform properties, and all variables, except pressure, are specified. At the outlet section, the pressure is prescribed and all other variables are extrapolated from the interior of the domain. The flow tangency condition is applied at the walls.

Figure 6*b* displays Mach contours over the domain, while Figure 6*c* presents a comparison between predicted Mach number values over the lower and upper walls of the domain with similar ones reported by Favini [40]. As shown, results are in excellent agreement.

The total computational cost, the cost per control volume, and the number of iterations required to obtain converged solutions over the five grid sizes used are presented in Table 1*c*. When using quadrilateral control volumes, the number required to obtain a converged solution for all grid sizes is between 20 and 22 iterations except for a grid with size of 50,000 Control Volumes (CV) where 32 iterations are required. For triangular elements, the number of iterations required with all grid sizes is 11 (except for the 10,000 CV grid where 13 iterations are needed). The CPU time per control volume varies between 6.00×10^{-3}s and 11.18×10^{-3}s for quadrilateral elements and between 2.0×10^{-3}s and 4.63×10^{-3}s for triangular elements.

Table 1. (*a*) Iterations and CPU time for subsonic flow over a NACA0012 airfoil ($M_\infty = 0.63, \alpha = 2°$), (*b*) Iterations and CPU time for transsonic flow over a NACA 0012 airfoil ($M_\infty = 0.85, \alpha = 1°$), (*c*) Iterations and CPU time for subsonic flow over a circular arc bump ($M_{\text{in}} = 0.5$), (*d*) Iterations and CPU time for flow over a circular arc bump (transconic, $M_{in} = 0.675$), (*e*) Iterations and CPU time for flow over a circular arc bump (supersonic, $M_{\text{in}} = 1.4$), (*f*) Iterations and CPU time for flow over a circular arc bump (supersonic, $M_{\text{in}} = 1.65$)

Quadrilateral elements				Triangular elements			
Grid Size	No. of #Iter.	*CPU*(*s*)	CPU/CV	Grid Size	No. of #Iter.	*CPU*(*s*)	CPU/CV
			(*a*)				
34,000	24	233	6.85×10^{-3}	43,000	30	699	16.26×10^{-3}
136,000	43	3, 718	27.34×10^{-3}	120,000	32	2, 185	18.21×10^{-3}
406,000	48	12, 775	31.46×10^{-3}	370,000	79	16, 289	44.02×10^{-3}
			(*b*)				
34,000	117	1, 288	37.88×10^{-3}	43,000	35	393	9.14×10^{-3}
136,000	272	23, 470	172.57×10^{-3}	120,000	189	12, 884	107.37×10^{-3}
406,000	392	104, 116	256.44×10^{-3}	370,000	733	150, 690	407.27×10^{-3}
			(*c*)				
1,000	20	6	6.00×10^{-3}	1,000	11	2	2.00×10^{-3}
10,000	22	68	6.80×10^{-3}	10,000	13	39	3.9×10^{-3}
50,000	32	559	11.18×10^{-3}	50,000	11	212	4.24×10^{-3}
100,000	23	884	8.84×10^{-3}	100,000	11	434	4.34×10^{-3}
300,000	21	2, 830	9.43×10^{-3}	300,000	11	1, 390	4.63×10^{-3}
			(*d*)				
1,000	18	6	6.00×10^{-3}	1,000	16	3	3.00×10^{-3}
10,000	39	106	10.60×10^{-3}	10,000	19	57	5.7×10^{-3}
50,000	90	1, 340	26.80×10^{-3}	50,000	22	409	8.18×10^{-3}
100,000	135	4, 096	40.96×10^{-3}	100,000	100	2, 580	25.80×10^{-3}
300,000	97	7, 515	25.05×10^{-3}	323,000	85	6, 958	21.54×10^{-3}
			(*e*)				
10,000	24	67	6.70×10^{-3}	10,000	25	209	20.90×10^{-3}
66,000	31	595	9.02×10^{-3}	66,000	35	1, 246	18.88×10^{-3}
333,000	57	9, 870	29.64×10^{-3}	333,000	62	11, 538	34.65×10^{-3}
			(*f*)				
10,000	23	63	6.30×10^{-3}	10,000	20	167	16.70×10^{-3}
66,000	27	520	7.88×10^{-3}	66,000	24	851	12.89×10^{-3}
333,000	36	6, 221	18.68×10^{-3}	333,000	36	6, 631	19.91×10^{-3}

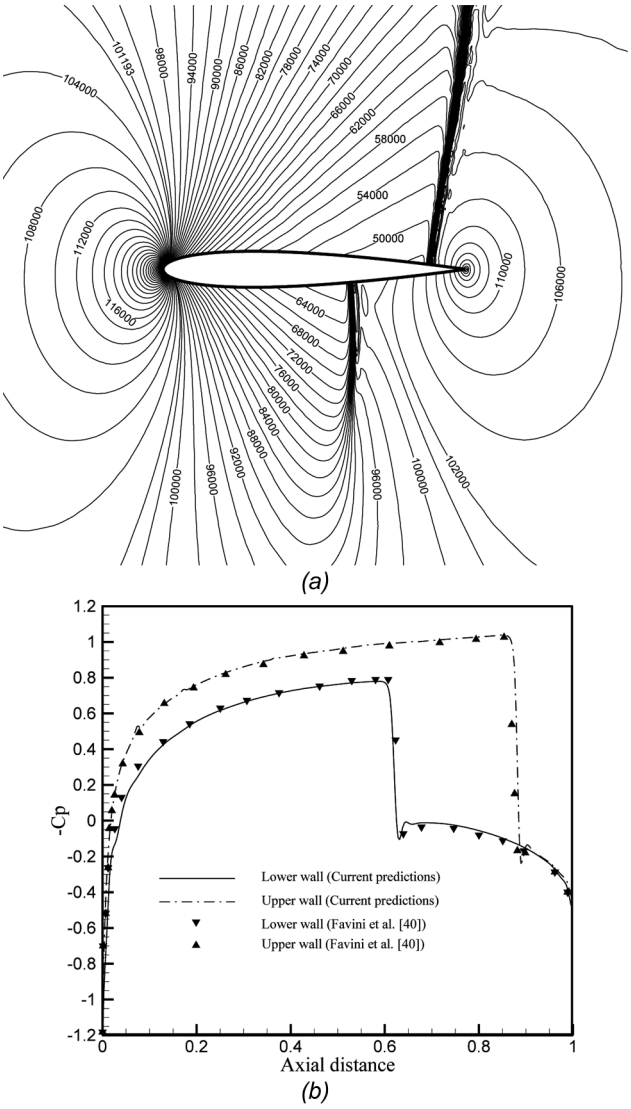

Figure 4. (*a*) Isobars and (*b*) comparison of predicted pressure coefficient values along the upper and lower surfaces of the airfoil with published data [40] for transsonic flow over a NACA 0012 airfoil ($M_\infty = 0.85, \alpha = 1°$).

The reduction of residuals with number of iterations for quadrilateral elements is depicted in Figures 7*a*–7*c*, while reduction for triangular elements is revealed in figures 7*d*–7*f*. As shown, for a given type of grid the convergence paths for all cases are similar.

Case 2: Transsonic flow over a circular arc bump. With the exception of the inlet Mach number being set at 0.675, the grid distribution and the

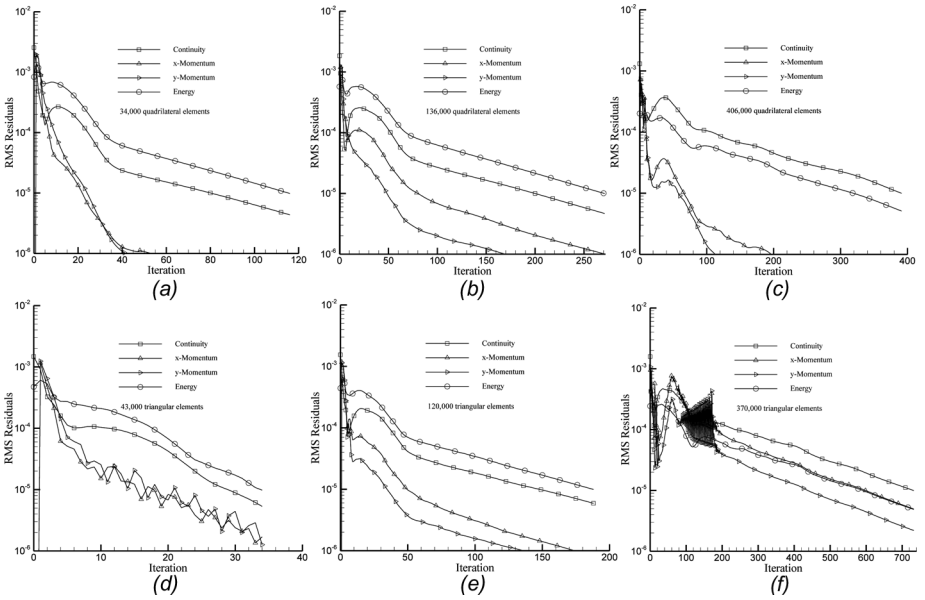

Figure 5. Convergence history for transsonic flow over a NACA0012 airfoil ($M_\infty = 0.85, \alpha = 1°$).

implementation of boundary conditions are identical to those described for subsonic flow. Results are displayed in terms of lines of constant Mach number over the domain Figure 8*a* and Mach profiles along the walls Figure 8*b*. Predicted profiles are compared with similar ones reported in [40] and shown to be in excellent agreement. In addition, the transonic nature of the flow is demonstrated by the formation of the shock wave, which is clearly shown in Figures 8*a* and 8*b*.

The performance of the coupled solver as the number of grid points increases can be inferred from the values presented in Table 1*d*. With quadrilateral control volumes, the number of iterations needed for convergence varies between 18 and 135. For triangular elements, the number varies between 16 and 100. The CPU time per control volume varies between 6.00×10^{-3}s and 40.96×10^{-3}s for quadrilateral elements and between 3.0×10^{-3}s and 25.8×10^{-3}s for triangular elements. The decrease in residuals with iteration is presented in Figures 9*a*–9*c* for grid systems using quadrilateral elements and in Figures 9*d*–9*f* for grid networks employing triangular elements. Plots indicate that the convergence paths are similar for a given type of elements.

Case 3: Supersonic flow over a circular arc bump. Computations are performed for two values of the inlet Mach number, 1.4 and 1.65. For these values and for the geometry used, the flow is also supersonic at the outlet. Thus, all variables at the inlet are prescribed, and at outlet all variables are extrapolated. Mach contours over the domain are presented in Figure 10*a* for $M_{in} = 1.65$, and in Figure 10*b* for $M_{in} = 1.4$. These contours are in excellent agreement with similar ones reported in the literature. For further confirmation, the predicted Mach values along the lower and upper walls are compared in Figure 10*c* with similar ones reported

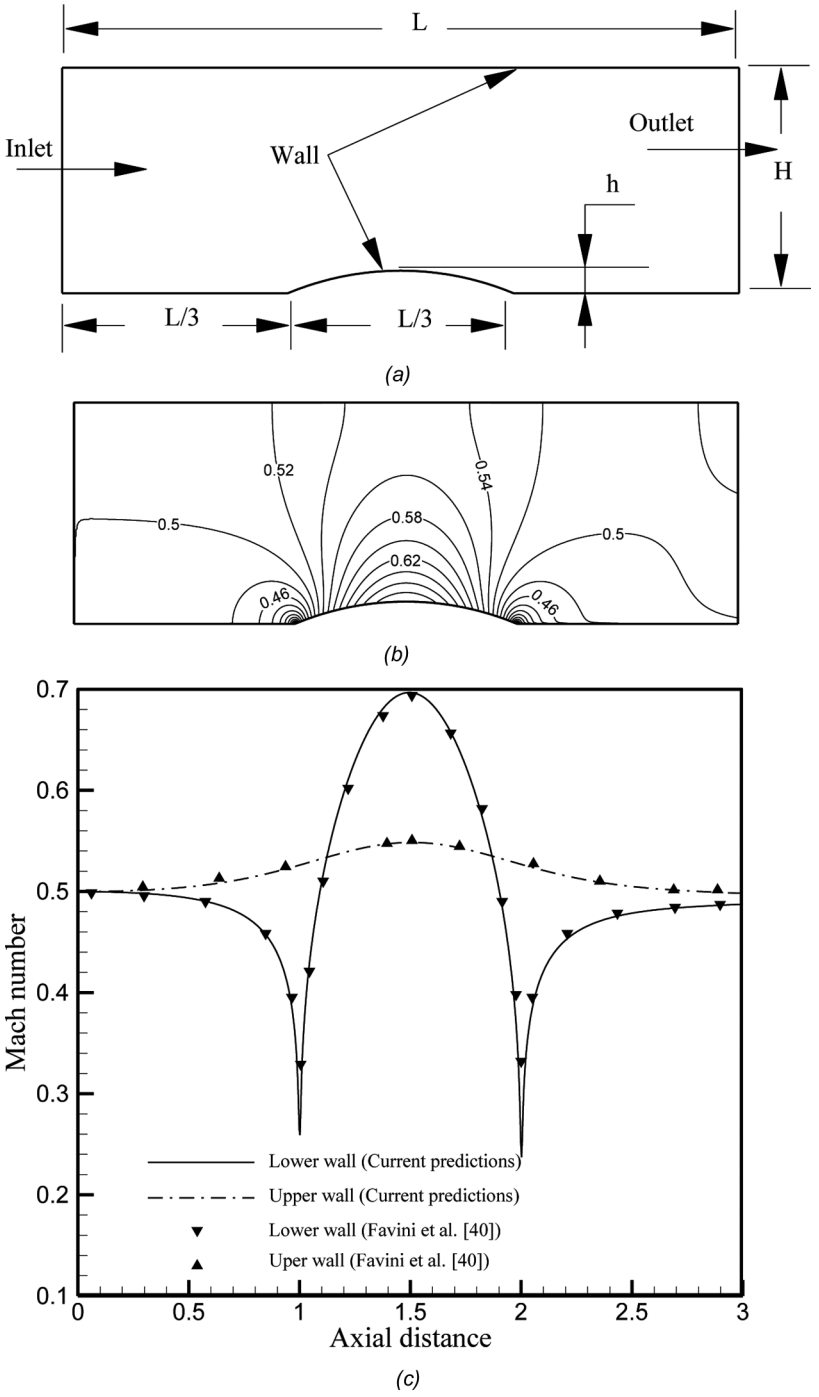

Figure 6. (*a*) Physical situation for the flow over a circular arc bump; (*b*) Mach contours for subsonic flow over a circular arc bump ($M_{in} = 0.5$); and (*c*) comparison of predicted Mach number values along the upper and lower walls with published data [40] ($M_{in} = 0.5$).

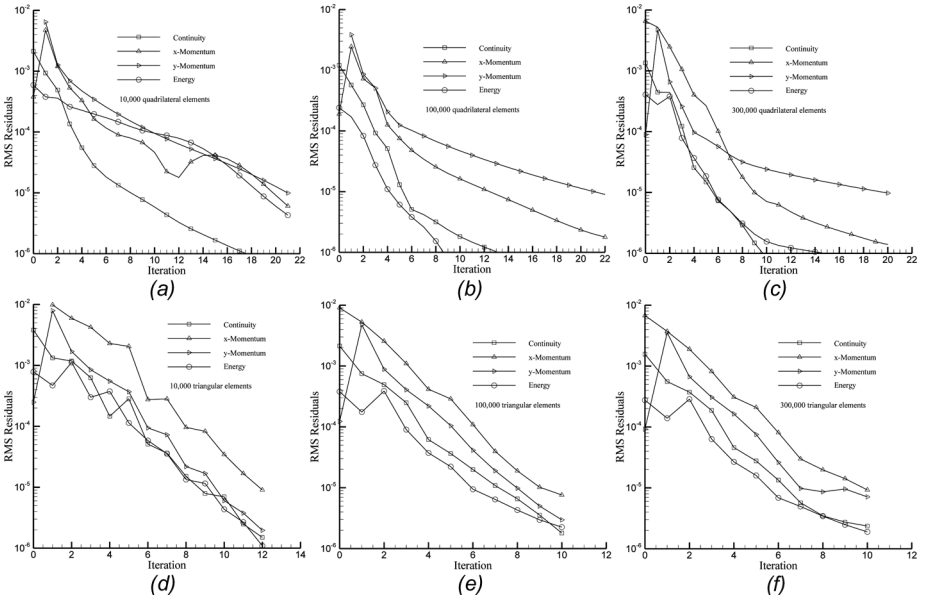

Figure 7. Convergence history for subsonic flow over a circular arc bump ($M_{\text{in}} = 0.5$).

in [40]. As shown, profiles are on top of each other, indicating once more the correct implementation of the coupled algorithm.

Results reported in Table 1*e* indicate that for $M_{in} = 1.4$ the number of iterations required for convergence varies between 24 and 57 as the number of quadrilateral elements increases from 10,000 to 333,000. The computational time per control volume varies between 6.70×10^{-3}s and 29.64×10^{-3}s. For triangular elements, the number of iterations varies between 25 and 62, while the CPU time per control volume changes between 20.90×10^{-3}s and 34.65×10^{-3}s as the number of grid points increases from 10,000 to 333,000. The convergence history is depicted in Figures 11*a*–11*c* for grid systems using quadrilateral elements and in Figures 11*d*–11*f* for grid networks employing triangular elements. Plots indicate that the convergence paths are to some extent similar for a given type of elements.

At the higher inlet Mach number ($M_{in} = 1.65$), convergence data over the various grid systems used are presented in Table 1*f*. As depicted, the number of iterations varies between 23, for a grid with size of 10,000 quadrilateral control volumes, and 36, for a grid with size of 333,000 quadrilateral/triangular control volumes. The CPU time increases from 63 s for the case of 10,000 quadrilateral control volumes to 6,631 s for the case of 333,000 triangular control volumes. Moreover, the CPU per control volume for a quadrilateral element increases from 6.30×10^{-3} s to 18.68×10^{-3}s when the grid size increases from 10,000 to 333,000 control volumes. This represents a 196.51% increase in the solution cost per control volume for 3,230 % increase in the mesh size. For a triangular element, the CPU per control volume increases from 16.70×10^{-3} s to 19.91×10^{-3} s as the grid size increases from 10,000 to 333,000 control volumes. The increase in computational cost in this case is 19.22% for 3230 % increase in mesh size. The convergence

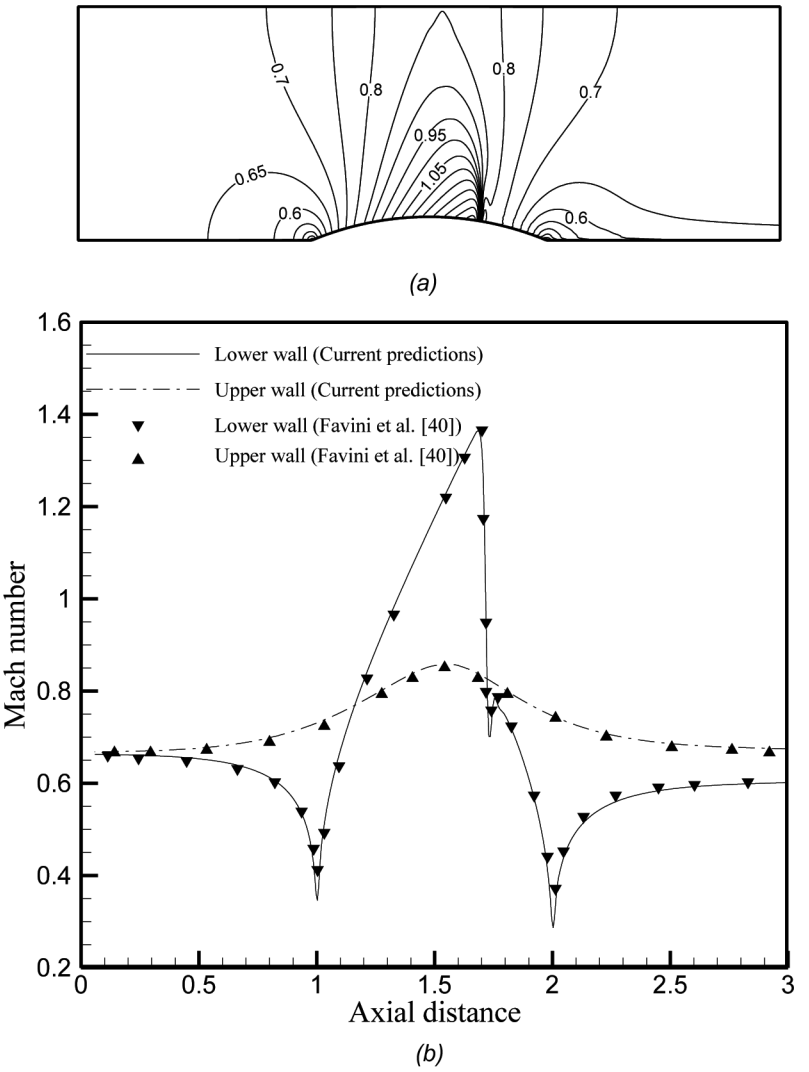

Figure 8. (*a*) Mach contours for transsonic flow over a circular arc bump ($M_{in} = 0.675$); and (*b*) comparison of predicted Mach number values along the upper and lower walls with published data [40] ($M_{in} = 0.675$).

history plots are displayed in Figures 12*a*–12*c* for grid networks using quadrilateral elements and in Figures 12*d*–12*f* for grid systems using triangular elements. Plots indicate that the convergence paths are mostly similar.

Problem 3: Supersonic Flow over an Obstacle

The physical situation is depicted in Figure 13*a* and represents a channel of height H and width W with a baffle of height $h = H/9$ mounted to its base and

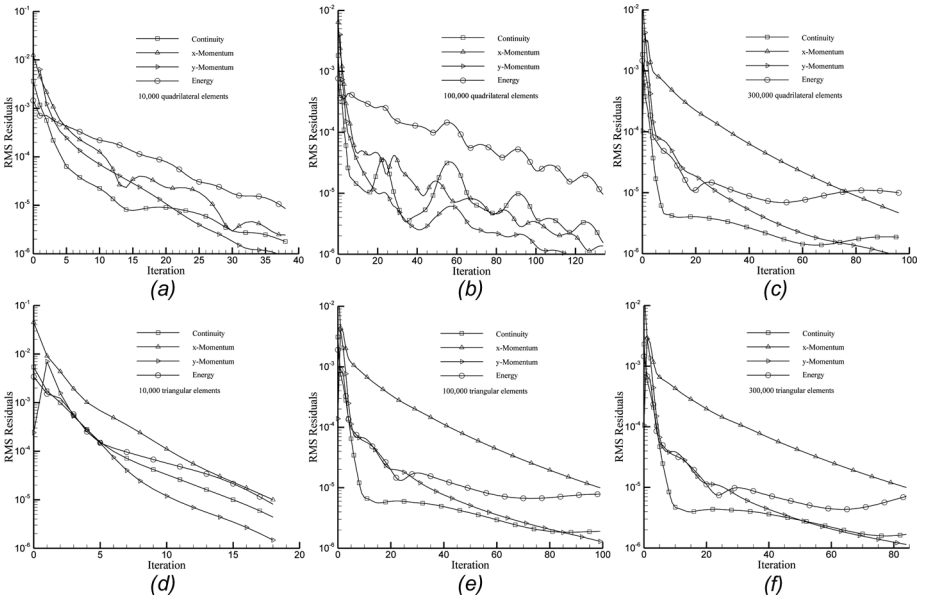

Figure 9. Convergence history for transsonic flow over a circular arc bump ($M_{\text{in}} = 0.675$).

located at its middle. Solutions are generated over a number of grid systems for the case when air enters the domain at a Mach number of 2 ($M_{in} = 2$). Predicted isobars are displayed in Figure 13*b*.

The convergence history plots are displayed in Figures 14*a*–14*c* for grid networks using quadrilateral elements and in Figures 14*d*–14*f* for grid systems using triangular elements. Plots indicate that for a given type of element, the convergence paths are similar for the different grid sizes. Moreover, plots in Figures 14*a*–14*c* show smooth convergence, whereas plots in Figures 14*d*–14*f* reveal a very rough convergence in the initial stage of the iterative process and then the convergence proceeds smoothly. To be noticed also is the greater number of iterations required for convergence to be reached, in comparison with the number required in the previous problems. This increase in computational cost is related to the complex structure of the flow.

Convergence data for the various grid systems used are presented in Table 2*a*. As depicted, the number of iterations varies between 180, for a grid with size of 10,092 quadrilateral elements, and 861, for a grid with size of 314,094 quadrilateral cells. Simultaneously the CPU time increases from 748 s for the case of 10,092 quadrilateral control volumes to 203,039 s for the case of 314,094 quadrilateral control volumes. Moreover, the CPU per control volume for a quadrilateral element increases from 74.12×10^{-3} s to 646.43×10^{-3}s when the grid size increases from 10,092 to 314,094 control volumes. This represents a 772.14% increase in the solution cost per control volume for 3,012.32% increase in the mesh size. For a triangular element, results displayed in Table 2*a* indicate that the CPU per control volume increases from 391.10×10^{-3}s to $1,225.1 \times 10^{-3}$s as the grid size increases

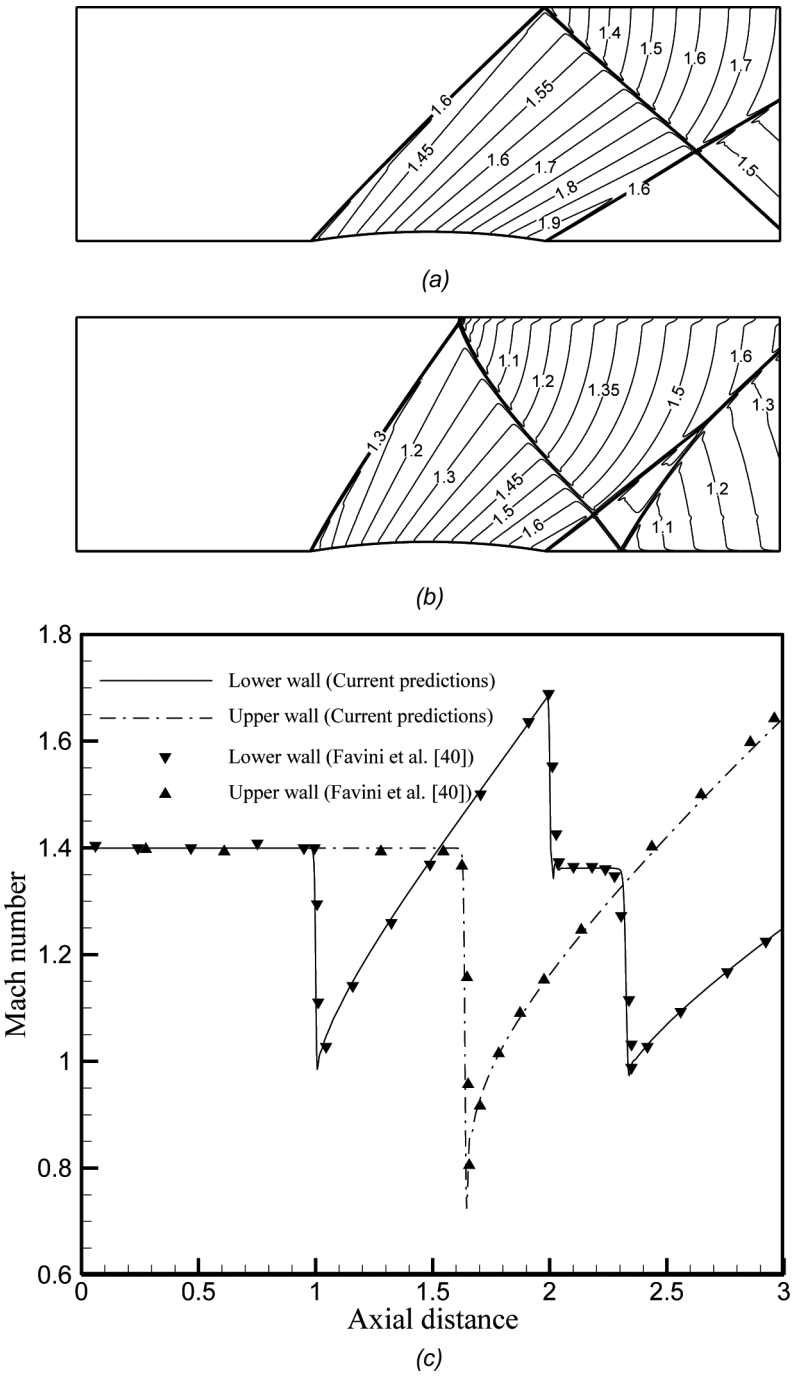

Figure 10. Mach contours for supersonic flow over a circular arc bump at (*a*) $M_{in} = 1.65$ and (*b*) $M_{in} = 1.4$; and (*c*) comparison of predicted Mach number values along the upper and lower walls with published data [40] ($M_{in} = 1.4$).

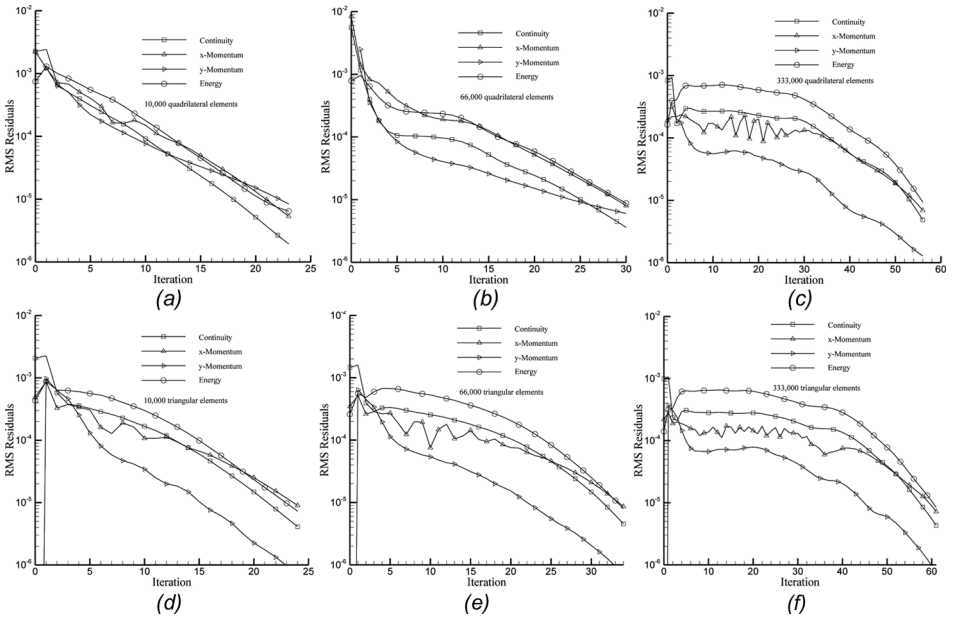

Figure 11. Convergence history for supersonic flow over a circular arc bump ($M_{\text{in}} = 1.4$).

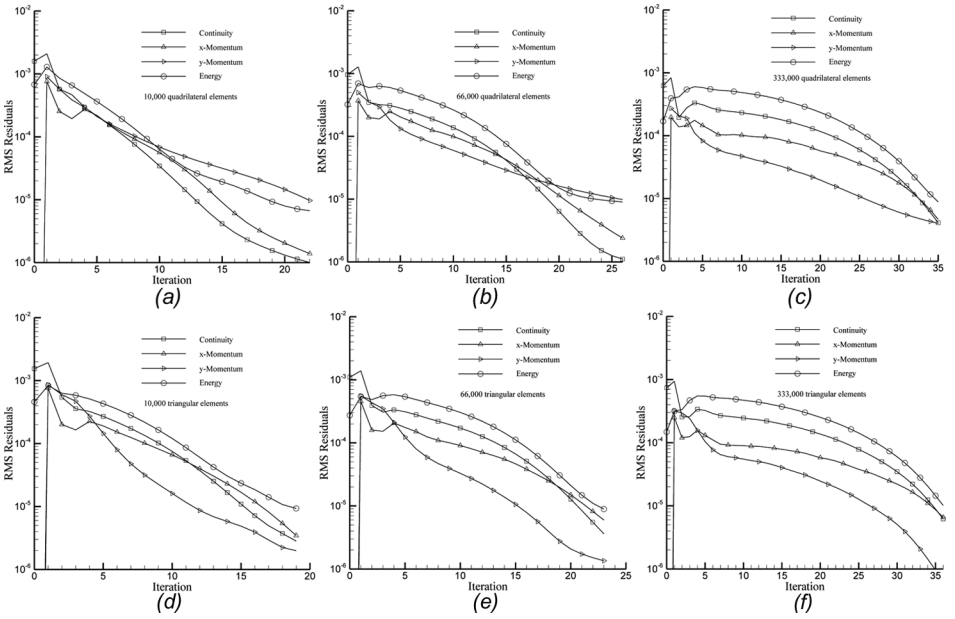

Figure 12. Convergence history for supersonic flow over a circular arc bump ($M_{\text{in}} = 1.65$).

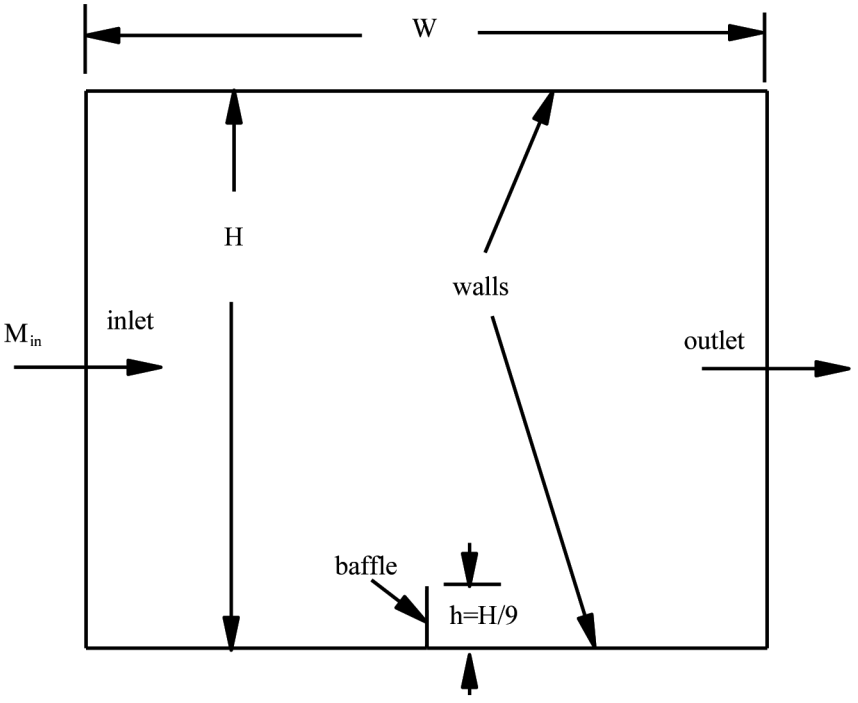

Figure 13. (*a*) Physical situation and (*b*) isobars for supersonic flow over an obstacle ($M_\infty = 2$).

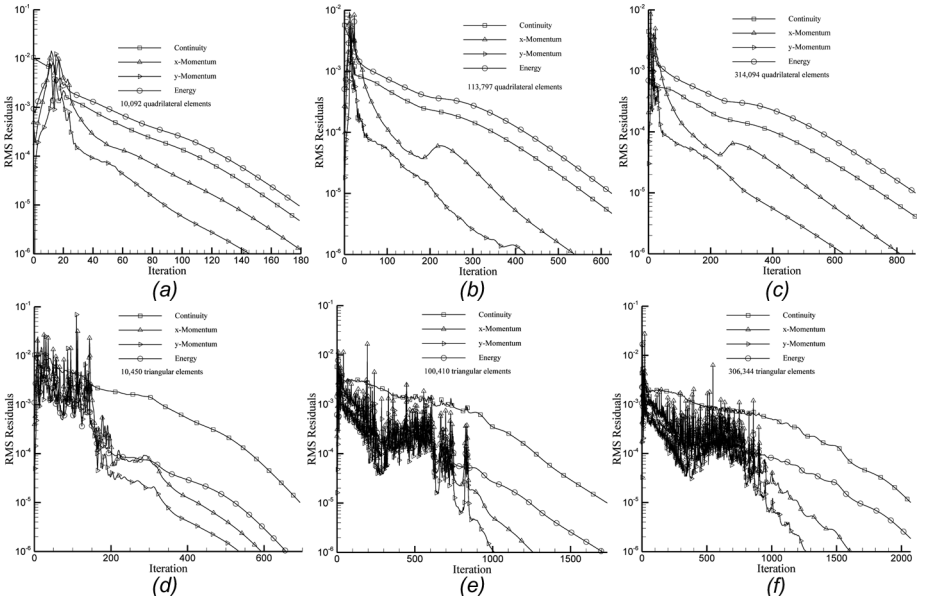

Figure 14. Convergence history for supersonic flow over an obstacle ($M_\infty = 2$).

from 10,450 to 306,344 control volumes. The increase in computational cost per control volume in this case is 213.24% for 2,831.52% increase in mesh size.

Problem 4: Supersonic Flow over a Circular Cylinder

In this problem, depicted schematically in Figure 15*a*, air is approaching a circular cylinder of radius $r = 1$ at a supersonic Mach number of 3 ($M_\infty = 3$). A uniform flow is assumed at inlet where all variables are specified. At the outlet, the flow is also supersonic and values of all variables are extrapolated from the interior. The slip condition is used on the cylinder wall. Solutions are generated using quadrilateral and triangular elements over three grid networks. An illustrative grid generated is depicted in Figure 15*b*. The problem has been solved by several researchers [40, 46–48], and the flow field is characterized by the formation of a detached shock wave at a distance d ahead of the cylinder, which can be evaluated by the approximate relation [49].

$$d = 0.386\, re^{4.67/M_\infty^2} \tag{34}$$

Results obtained using the coupled solver are displayed in the form of isobars and isotherms over the domain in Figures 15*c* and 15*d*, respectively. Results are in excellent agreement with similar ones reported in [40]. The shock along the centerline of the domain is numerically predicted to be located at $d = 0.609$, which is close to the value $d = 0.648$ evaluated using the approximate relation (34).

The problem is solved over several grid sizes, and convergence data are presented in Table 2*b*. Using quadrilateral elements, the number of iterations varies

between 95 and 284 as the grid size increases from 12,783 to 253,045 control volumes. For triangular elements it varies between 150 and 325 as the grid size increases from 12,766 to 246,594 elements. The computational time increases for quadrilateral elements from 430 s to 28,026 s and for triangular elements from 611 s to 29,027 s as the grid size increases. Moreover, the CPU per control volume for a quadrilateral element increases from 33.64×10^{-3} s to 110.76×10^{-3} s when the grid size increases from 12,783 to 253,045 control volumes. This represents a 229.25% increase in the solution cost per control volume for 1,879.54 % increase in the mesh size. For a triangular element, the CPU per control volume increases from 47.86×10^{-3} s to 117.71×10^{-3} s as the grid size increases from 12,766 to 246,594 control volumes. The increase in computational cost in this case is 145.94% for 1831.65 % increase in mesh size. The convergence history plots are displayed in Figures 16*a*–16*c* for grid networks using quadrilateral elements and in Figures 16*d*–16*f* for grid systems using triangular elements. As depicted, a smooth convergence is obtained with quadrilateral elements, while the convergence behavior when using

Table 2. (*a*) Iterations and CPU time for supersonic flow over an obstacle ($M_\infty = 2$), (*b*) Iterations and CPU time for supersonic flow over a circular cylinder ($M_\infty = 3$), (*c*) Iterations and CPU time for hypersonic flow over a wedge ($\alpha = 15°$, $M_\infty = 10$), (*d*) Iterations and CPU time for transonic flow in a converging-diverging nozzle [subsonic inlet at ($M_{in} = 0.3$), supersonic at outlet], (*e*) Iterations and CPU time for transsonic flow in a converging-diverging nozzle with a normal shock wave at $x = 7$ [subsonic inlet ($M_{in} = 0.3$), subsonic at outlet]

Quadrilateral elements				Triangular elements			
Grid Size	No. of #Iter.	*CPU*(*s*)	CPU/CV	Grid Size	No. of #Iter.	*CPU*(*s*)	CPU/CV
			(*a*)				
10,092	180	748	74.12×10^{-3}	10,450	695	4, 087	391.10×10^{-3}
113,797	626	32, 866	288.81×10^{-3}	100,410	1, 737	108, 727	1082.8×10^{-3}
314,094	861	203, 039	646.43×10^{-3}	306,344	2, 071	375, 316	1225.1×10^{-3}
			(*b*)				
12,783	95	430	33.64×10^{-3}	12,766	150	611	47.86×10^{-3}
80,159	208	8, 192	102.20×10^{-3}	79,218	230	8, 339	105.27×10^{-3}
140,601	212	11, 494	81.75×10^{-3}	148,054	273	14, 580	98.48×10^{-3}
253,045	284	28, 026	110.76×10^{-3}	246,594	325	29, 027	117.71×10^{-3}
			(*c*)				
19,404	54	275	14.17×10^{-3}	39,470	84	953	24.14×10^{-3}
53,760	74	1, 091	20.29×10^{-3}	193,856	117	8, 157	42.08×10^{-3}
483,072	127	18, 148	37.57×10^{-3}	336,790	141	17, 849	53.00×10^{-3}
			(*d*)				
10,000	45	86	8.60×10^{-3}	10,000	62	114	11.40×10^{-3}
100,000	140	3, 331	33.31×10^{-3}	100,000	168	3, 786	37.86×10^{-3}
300,000	217	15, 304	51.01×10^{-3}	300,000	270	19, 605	65.35×10^{-3}
			(*e*)				
10,000	108	204	20.40×10^{-3}	10,000	185	364	36.40×10^{-3}
100,000	430	10, 441	104.41×10^{-3}	100,000	431	10, 072	100.72×10^{-3}
300,000	823	60, 061	200.20×10^{-3}	300,000	524	39, 082	130.27×10^{-3}

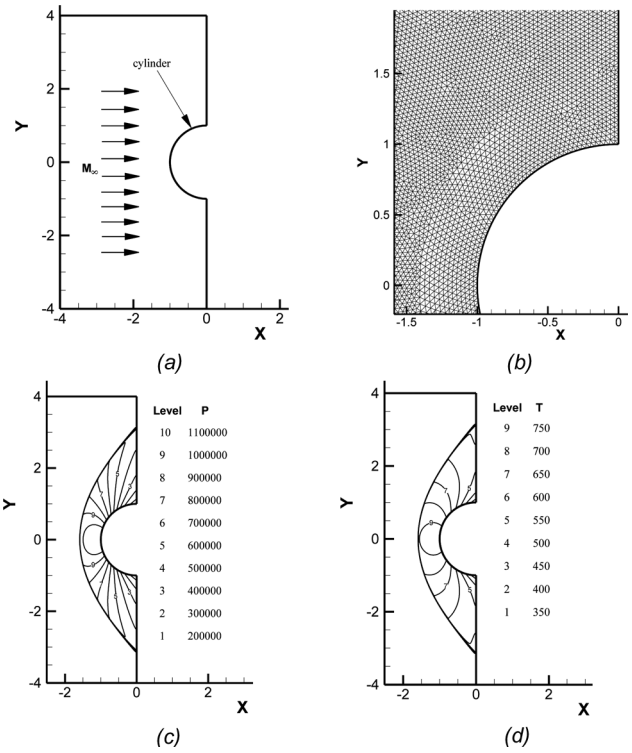

Figure 15. (*a*) Physical situation, (*b*) an illustrative grid over portion of the domain, (*c*) isobars, and (*d*) isotherms for supersonic flow over a circular cylinder ($M_\infty = 3$).

triangular elements shows some oscillations even though the number of iterations is close to that required by the corresponding cases using quadrilateral elements.

Problem 5: Hypersonic Flow over a Wedge

The physical domain is displayed schematically in Figure 17*a* and represents a free stream of air approaching a 15° wedge at hypersonic speed ($M_\infty = 10$). The surface including the compression corner forms the lower boundary. The inflow boundary is placed at $x = 0$ and the outflow boundary is at $x = 1.5$. The upper boundary is chosen to be located at a height $y = 1.26$. The problem has been used as a benchmark by several researchers [50–53], as a one-dimensional analytical solution to the problem exists. If the Mach number is high enough and the wedge angle is small enough, an oblique shock wave is generated by the wedge, with the origin of the shock attached to the sharp leading edge of the wedge. For a given upstream Mach number M_∞, there is a maximum wedge angle for which the shock remains attached to the leading edge and is given by [54, 55]

$$\alpha < \frac{4}{3\sqrt{3}\,(\gamma+1)} \frac{\left(M_\infty^2 - 1\right)^{3/2}}{M_\infty^2} \tag{35}$$

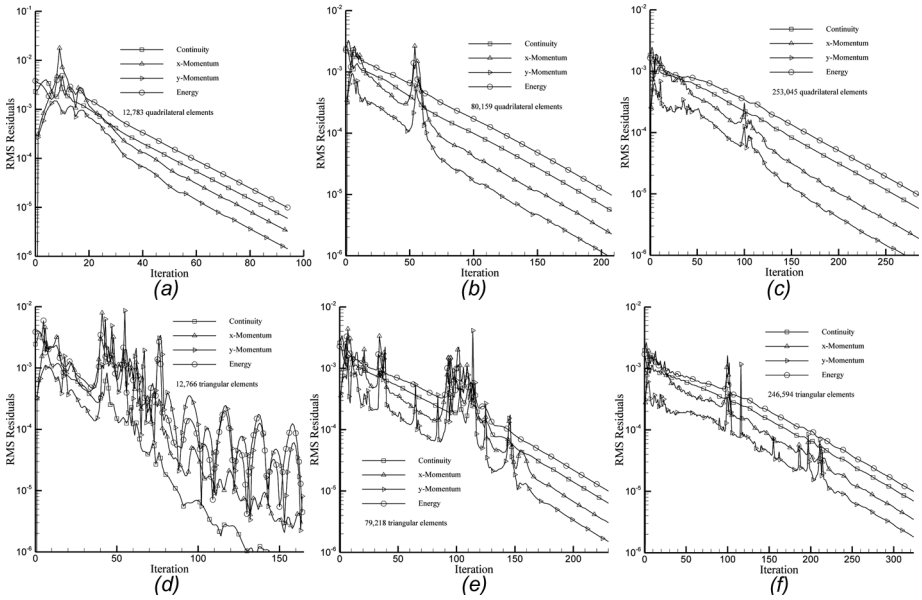

Figure 16. Convergence history for supersonic flow over a circular cylinder ($M_\infty = 3$).

For wedge angles greater than the maximum, a detached normal shock occurs. The upstream Mach number and wedge angle considered result in an oblique shock wave attached to the leading edge of the wedge. In this case, the analytical solution to the problem is given by

$$\cot(\alpha) = \tan(s)\left[\frac{0.5(\gamma+1)M_\infty^2}{M_\infty^2 \sin^2(s) - 1} - 1\right] \tag{36}$$

$$M_1^2 \sin^2(s-\alpha) = \frac{(\gamma-1)M_\infty^2 \sin^2(s) + 2}{2\gamma M_\infty^2 \sin^2(s) - (\gamma-1)} \tag{37}$$

where s is the shock angle, M_1 the Mach number after the shock, and γ the specific heat ratio. Again the problem is solved using several grid systems of increasing density, and the resulting streamlines and oblique shock wave are displayed in Figure 17*b*. Based on Eqs. (36) and (37), the shock angle and Mach number after the shock are $s = 19.94°$ and $M_1 = 5.28$. The values obtained numerically are $s = 19.61°$ and $M_1 = 5.5$, which are close to the analytical values given that the convective flux is discretized with the upwind scheme and the grid is uniformly distributed over the domain with no concentration in the region around the shock.

The convergence data are presented in Table 2*c*. Using quadrilateral elements, the problem is solved using three grid systems with sizes varying between 19,404 and 483,072 control volumes. Results in Table 2*c* indicate that the number of iterations varies between 54 and 127 and the CPU per control volume increases from 14.17×10^{-3} s to 37.57×10^{-3} s. This represents an increase of 165.14% in computational cost per control volume for 2,389.55% increase in grid size. For

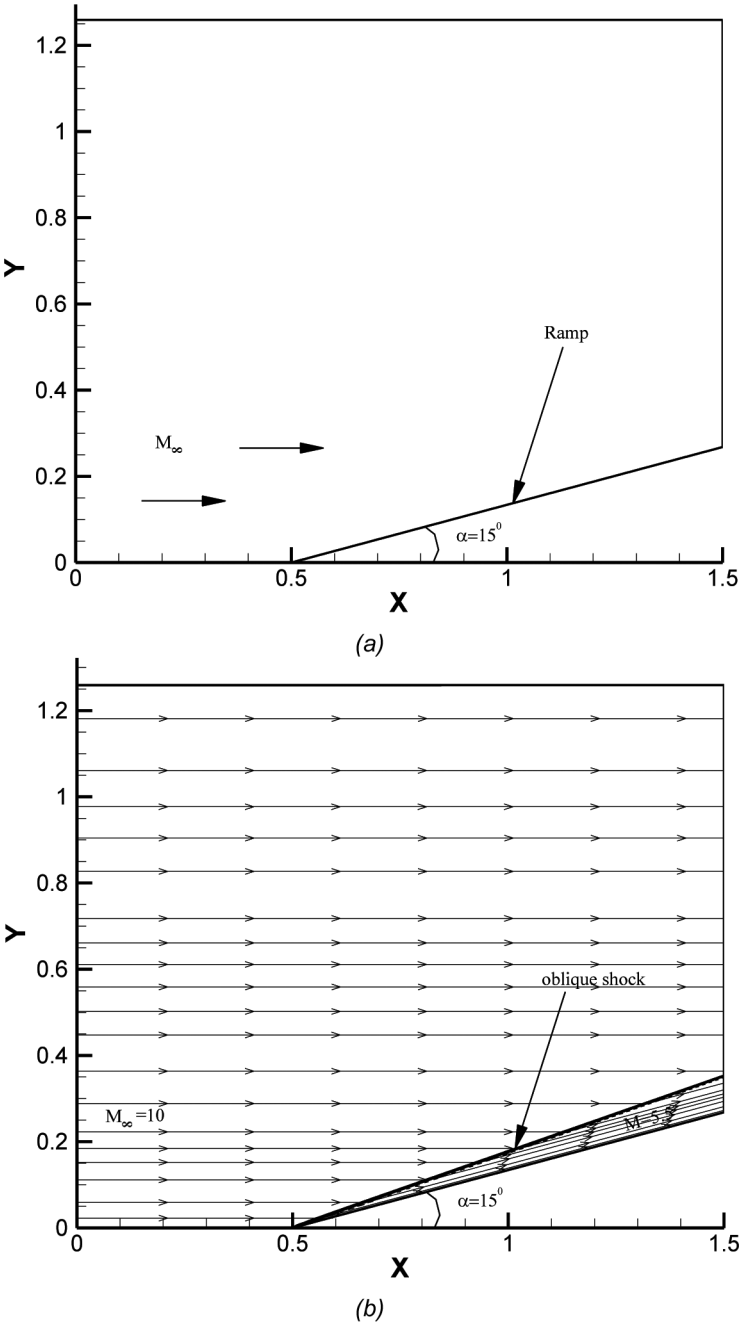

Figure 17. (*a*) Physical situation and (*b*) streamlines for hypersonic flow over a wedge.

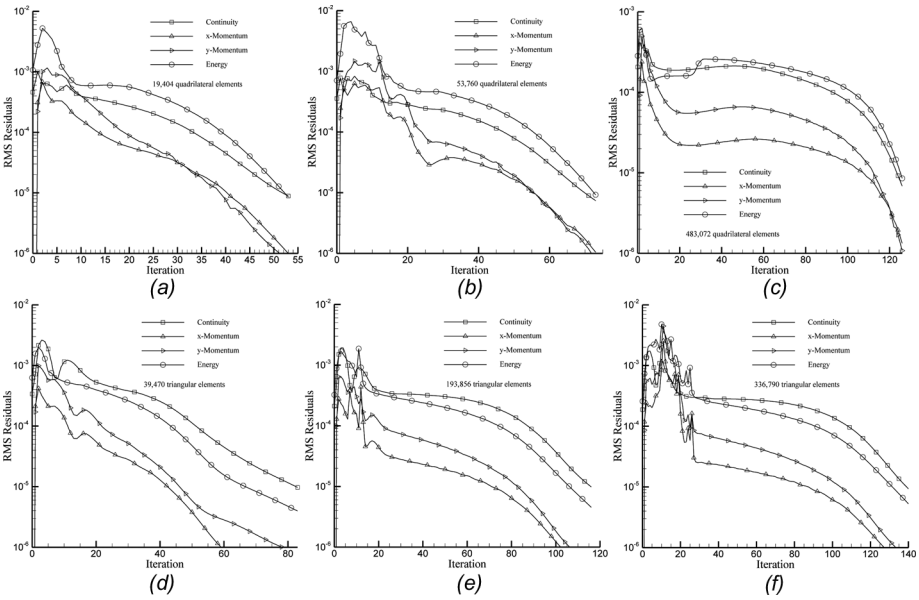

Figure 18. Convergence history for hypersonic flow over a wedge ($M_\infty = 10$).

triangular elements, the number of iterations increases from 84 to 141 as the grid size increases from 39,470 to 336,790 cells. The cost per control volume increases by 119.55% with an increase of 753.28% in the grid size. The convergence history plots are displayed in Figures 18*a*–18*c* for grid networks using quadrilateral elements and in Figures 18*d*–18*f* for grid systems using triangular elements. As depicted, a smooth convergence is obtained with both quadrilateral and triangular elements, with similar convergence history plots.

Problem 6: Flow in a Converging-Diverging Nozzle

The test selected, shown schematically in Figure 19*a*, is a standard one that has been used by several researchers for comparison purposes [10, 45, 56] and represents the flow in a converging-diverging nozzle with its cross-sectional area varying according to

$$S_{(x)} = S_{\text{th}} + (S_i - S_{\text{th}}) \left(1 - \frac{x}{5}\right)^2 \tag{38}$$

where $S_i = 2.035$ and $S_{\text{th}} = 1$ are the inlet and throat areas, respectively, and $0 \leq x \leq 10$. Solutions are obtained for an inlet Mach number of 0.3 ($M_{in} = 0.3$) for two values of the back pressure resulting either in a supersonic flow at exit or in the formation of a normal shock wave at $x = 7$. Two-dimensional numerical results for the two cases considered are compared in terms of area-weighted pressure values with one-dimensional analytical solutions in Figures 19*b* and 19*c* and are shown to be in excellent agreement with numerical values, falling on top of the analytical ones.

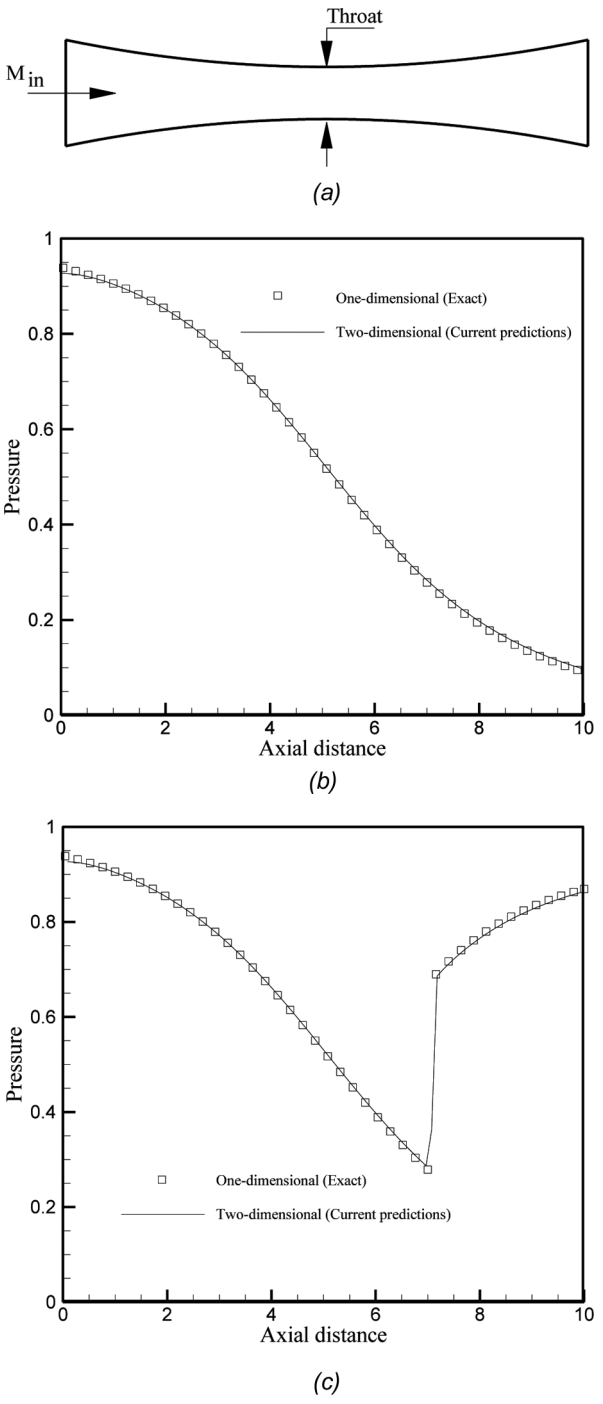

Figure 19. (*a*) Physical situation and (*b*, *c*) comparison of predicted pressure values with analytical ones for the flow in a converging-diverging nozzle with either (*b*) supersonic flow at exit or (*c*) formation of a shock wave at $x = 7$.

A summary of the computational data is reported in Table 2*d* for the case when the flow is supersonic in the entire diverging section of the nozzle and in Table 2*e* for the case when a shock wave is formed at $x = 7$. As shown in Table 2*d* the number of iterations increases from 45 to 217 and from 62 to 270 as the grid size increases from 10,000 to 300,000 control volumes with quadrilateral and triangular elements, respectively. The CPU per cell increases by 493.14% and 473.25% as the grid increases by 2,900% for quadrilateral and triangular elements, respectively. When a shock develops in the domain Table 2*e*, the number of iterations varies between 108 and 823 for quadrilateral elements and between 185 and 524 for triangular elements. The cost per control volume increases by 881.37% for quadrilateral elements and 257.88% for triangular elements as the grid size increases by 2,900%.

The convergence history plots are displayed in Figures 20 and 21 for the case when the flow at the exit from the nozzle is supersonic and when a shock wave is present, respectively. For fully supersonic flow in the diverging section, convergence histories are displayed in Figures 20*a*–20*c* for grid networks using quadrilateral elements and in Figures 20*d*–20*f* for grid systems using triangular elements. As depicted, curves are very similar and indicate that convergence starts slow until a good initial guess is obtained, beyond which residuals drop very quickly. For the case when a shock occurs in the diverging section Figures 21*a*–21*f*, a cyclic reduction in the residuals is noticed while the solver is trying to home on the exact location of the shock. For a given grid size, the convergence behavior is seen to be almost independent of the type of element used.

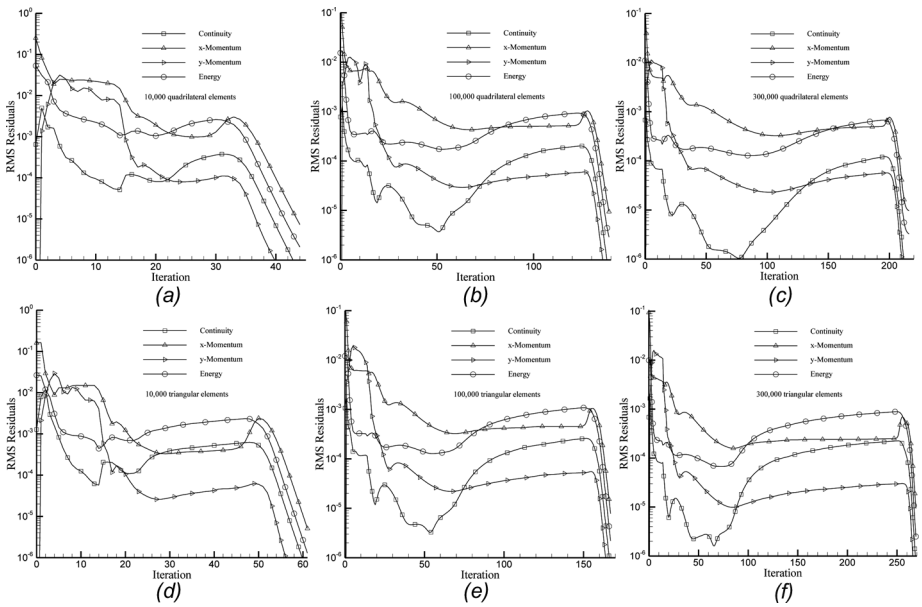

Figure 20. Convergence history for transsonic flow in a converging-diverging nozzle [subsonic inlet ($M_{\text{in}} = 0.3$], supersonic at outlet).

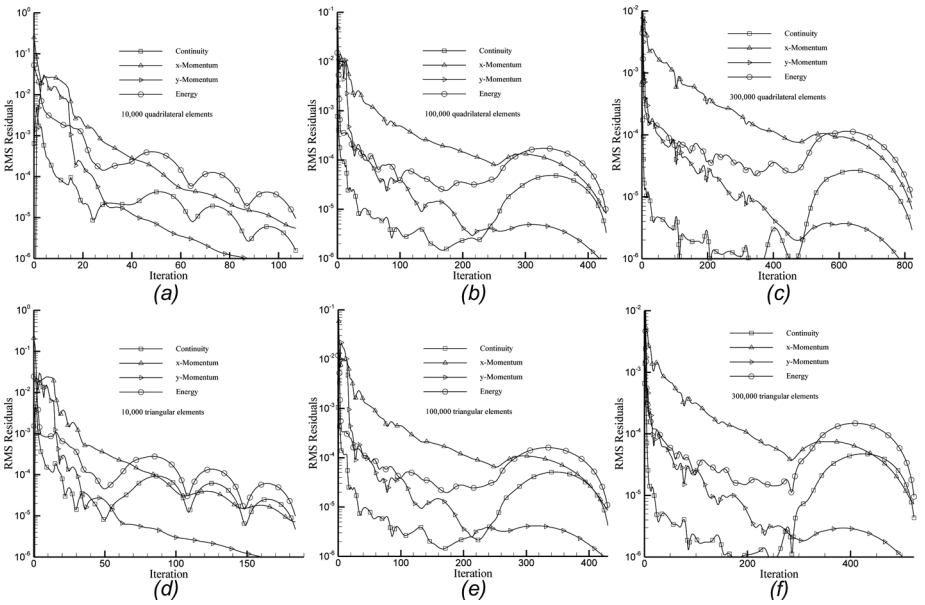

Figure 21. Convergence history for transsonic flow in a converging-diverging nozzle with a normal shock wave at $x = 7$ ($M_{\text{in}} = 0.3$).

CLOSING REMARKS

A newly developed, fully coupled, pressure-based algorithm for the solution of incompressible and compressible flow problems was presented. The performance of the solver was assessed by presenting solutions to several flow problems with speeds varying from low subsonic to hypersonic values. For each problem, solutions were generated over several grid systems ranging from 10,000 to almost 400,000 control volumes. Results presented in the form of convergence history plots, required number of iterations, total CPU time, and CPU time per control volume demonstrated the robustness and high stability of the solver.

REFERENCES

1. S. V. Patankar and D. B. Spalding, A Calculation Procedure for Heat, Mass and Momentum Transfer in Three-Dimensional Parabolic Flows, *Int. J. Heat Mass Transfer*, vol. 15, pp. 1787–1806, 1972.
2. J. P. Van Doormaal and G. D. Raithby, Enhancement of the SIMPLE Method for Predicting Incompressible Fluid Flows, *Numeri. Heat Transfer*, vol. 7, pp. 147–163, 1984.
3. C. M. Rhie and W. L. Chow, A Numerical Study of the Turbulent Flow past an Isolated Airfoil with Trailing Edge Separation, *AIAA J.*, vol. 21, pp. 1525–1532, 1983.
4. K. C. Karki, A Calculation Procedure for Viscous Flows at All Speeds in Complex Geometries, Ph.D. thesis, University of Minnesota, June 1986.
5. C. H. Marchi and C. R. Maliska, A Non-orthogonal Finite-Volume Method for the Solution of All Speed Flows Using Co-located Variables, *Numer. Heat Transfer B,* vol. 26, pp. 293–311, 1994.

6. F. S. Lien and M. A. Leschziner, A General Non-orthogonal Collocated Finite Volume Algorithm for Turbulent Flow at All Speeds Incorporating Second-Moment Turbulence-Transport Closure, Part 1: Computational Implementation, *Comput. Meth. Appl. Mech. Eng.*, vol. 114, pp. 123–148, 1994.
7. K. S. Shterev and S. K. Stefanov, Pressure Based Finite Volume Method for Calculation of Compressible Viscous Gas Flows, *J. Comput. Phys.*, vol. 229, no. 2, pp. 461–480, 2010.
8. Y. Moguen, E. Dick, J. Vierendeels, and P. Bruel, Pressure Velocity Coupling for Unsteady Low Mach Number Flow Simulations: An Improvement of the AUSM Scheme, *J. Comput. Appl. Math.*, vol. 246, pp. 136–143, 2013.
9. F. Moukalled and M. Darwish, A Unified Formulation of the Segregated Class of Algorithms for Fluid Flow at All Speeds, *Numer. Heat Transfer B,* vol. 37, pp. 103–139, 2000.
10. F. Moukalled and M. Darwish, A High Resolution Pressure-Based Algorithm for Fluid Flow at All-Speeds, *J. Comput. Phys.*, vol. 169, pp. 101–133, 2001.
11. M. Darwish, F. Moukalled, and B. Sekar, A Unified Formulation for the Segregated Class of Algorithms for Multi-fluid Flow at All Speeds, *Numer. Heat Transfer B,* vol. 40, pp. 99–137, 2001.
12. F. Moukalled and M. Darwish, A High Resolution Pressure Based Algorithm for Multiphase Flow at All Speeds, *J. Comput. Phys.*, vol. 168, pp. 101–133, 2002.
13. S. Muzaferija and D. Gosman, Finite-Volume CFD Procedure and Adaptive Error Control Strategy for Grids of Arbitrary Topology, *J. Comput. Phys.*, vol. 138, pp. 766–787, 1997.
14. R. B. Langtry and F. Menter, Transition Modeling for General CFD Applications in Aeronautics, AIAA Paper 2005–522, 2005.
15. F. R. Menter, M. Kuntz, and R. Langtry, Ten Years of Industrial Experience with the SST, Turbulence Model, in K. Hanjalic, Y. Nagano, and M, Tummers (eds.), *Turbulence, Heat and Mass Transfer 4*, Begell House, New york, 2003.
16. L. Zhang, W. Zhao, and X. Shao, A Pressure-Based Algorithm for Cavitating Flow Computations, *J. Hydrodynam.*, Ser. B, vol. 23, no. 1, pp 42–47, 2011.
17. W. Dettmer, D. Peric, A Computational Framework for Free Surface Fluid Flows Accounting for Surface Tension, *Comput. Meth. Appl. Mech. Eng.*, vol. 195, pp. 3038–3071, 2006.
18. A. Cabboussat, M. Picasso, and J. Rappaz, Numerical Simulation of Free Surface Incompressible Liquid Flows Surrounded by Compressible Gas, *J. Comput. Phys.*, vol. 203, pp. 626–649, 2005.
19. F. Moukalled and M. Darwish, A Comparative Assessment of the Performance of Mass Conservation Based Algorithms for Incompressible Multi-phase Flows, *Numer. Heat Transfer B,* vol. 42, pp. 259–283, 2002.
20. F. Moukalled, M. Darwish, and B. Sekar, A Pressure-Based Algorithm for Multi-phase Flow at All Speeds, *J. Comput. Phys.*, vol. 190, pp. 550–571, 2003.
21. F. Moukalled and M. Darwish, The Performance of Geometric Conservation–Based Algorithms for Incompressible Multifluid Flow, *Numer. Heat Transfer B,* vol. 45, pp. 343–368, 2004.
22. I. E. Barton, Comparison of SIMPLE- and PISO-Type Algorithms for Transient Flows, *Int. J. Numer. Meth. Fluids*, vol. 26, pp. 459–483, 1998.
23. V. A. O. Anjorin and I. E. Barton, Removal of Temporal and Under-relaxation Terms from the Pressure-Correction Equation of the SIMPLE Algorithm, *Int. J. Fluid Dynam.*, vol. 5, no. 5, pp 59–75, 2001.
24. S. Acharya, B. R. Baliga, K. Karki, J. Y. Murthy, C. Prakash, and P. Vanek, Pressure Based Finite Volume Methods in Computational Fluid Dynamics, *J. Heat Transfer*, vol. 129, pp. 407–424, 2007.

25. W. Q. Tao, Z. G. Qu, and Y. L. He, A Novel Segregated Algorithm for Incompressible Fluid Flow and Heat Transfer Problems—CLEAR (Coupled and Linked Equations Algorithm Revised) Part I: Mathematical Formulation and Solution Procedure, *Numer. Heat Transfer B,* vol. 45, pp. 1–17, 2004.
26. R. Abbasi, A. Ashrafizadeh, and A. Shadaram, A Comparative Study of Finite Volume Pressure- Correction Projection Methods on Co-located Grid Arrangements, *Comput. Fluids*, vol. 81, pp. 68–84, 2013.
27. M. Darwish, F. Moukalled, and B. Sekar A Robust Multigrid Pressure Based Algorithm for Multifluid Flow at All Speeds, *Int. J. Numeri. Meth. Fluids*, vol. 41, pp. 1221–1251, 2003.
28. M. Darwish, D. Asmar, and F. Moukalled, A Comparative Assessment within a Multigrid Environment of Segregated Pressure Based Algorithms for Fluid Flow at All Speeds, *Numer. Heat Transfer B,* vol. 45, pp. 49–74, 2004.
29. R. S. Montero and M. L. Ignacio, Robust Multigrid Algorithms for the Incompressible Navier-Stokes Equations," NASA ICASE Report 2000-27, 2000.
30. C. Hirsch, *Numerical Computation of Internal and External Flows*, John Wiley, New york, 1990.
31. E. Shapiro and D. Drikakis, Artificial Compressibility, Characteristics-Based Schemes for Variable Density, Incompressible Multispecies Flows. Part I. Derivation of Different Formulations and Constant Density Limit, *J. Comput. Phys.*, vol. 210, pp. 584–607, 2005.
32. C. Rossow, Efficient Computation of Compressible and Incompressible Flows, *J. Comput. Phys.*, vol. 220, pp. 879–899, 2007.
33. L. S. Caretto, R. M. Curr, and D. B. Spalding, Two Numerical Methods for Three-Dimensional Boundary Layers, *Comput. Meth. Appl. Mech. Eng.*, vol. 1, pp. 39–57, 1972.
34. K. Kissling, J. Springer, H. Jasak, S. Schutz, K. Urban, and M. Piesche, A Coupled Pressure Based Solution Algorithm Based on the Volume-of-Fluid Approach for Two or More Immiscible Fluids, in J. C. F. Pereira and A. Sequeira (eds.) *V European Conference on Computational Fluid Dynamics, ECCOMAS CFD 2010*, Lisbon, Portugal, 14–17 June 2010.
35. B. G. M. van Wachem and V. R. Gopala, A Coupled Solver Approach for Multiphase Flow Calculations on Collocated Grids, in P. Wesseling, E. Onate, and J. Periaux (eds.) *European Conference on Computational Fluid Dynamics, ECCOMAS CFD 2006*, Technical university of Delft, The Netherlands, 2006.
36. B. G. M. van Wachem, A. Benavides, and V. R. Gopala, A Coupled Solver Approach for Multiphase Flow Problems, in *6th International Conference on Multiphase Flow, ICMF 2007*, Leipzig, Germany, July 9–13, 2007.
37. G. B. Deng, J. Piquet, X. Vasseur, and M. Visonneau, A New Fully Coupled Method for Computing Turbulent Flows, *Comput. Fluids*, vol. 30, pp. 445–472, 2001.
38. M. Darwish, I. Sraj, and F. Moukalled, A Coupled Finite Volume Solver for the Solution of Incompressible Flows on Unstructured Grids, *J. Comput. Phys.*, vol. 228, pp. 180–201, 2009.
39. M. Darwish, I. Sraj, and F. Moukalled, A Coupled Incompressible Flow Solver on Structured Grids, *Numer. Heat Transfer B,* vol. 52, pp. 353–371, 2007.
40. B. Favini, R. Broglia, and A. Di Mascio, Multigrid Acceleration of Second-Order ENO Schemes from Low Subsonic to High Supersonic Flows, *Int. J. Numer. Meth. Fluids*, vol. 23, pp. 589–606, 1996.
41. C. J. Hwang and S. J. Wu, Adaptive Finite Volume Upwind Approach on Mixed Quadrilateral–Triangular Meshes, *AIAA J.*, vol. 31, pp. 61–67, 1993.
42. J. Y. Yang, Y. C. Perng, and R. H. Yen, Implicit Weighted Essentially Non-oscillatory Schemes for the Navier-Stokes Equations, *AIAA J.*, vol. 39, pp. 2082–2090, 2001.
43. J. T. Batina, Implicit Flux-Split Euler Schemes for UnsteadyAerodynamic Analysis Involving Unstructured Dynamic Meshes, *AIAA J.*, vol. 29, pp. 1836–1843, 1991.

44. Y. Yaldin and D. Caughy, Block Multigrid Implicit Solution ofthe Euler Equations of Compressible Fluid Flow, *AIAA J.*, vol. 29, pp. 712–719, 1991.
45. I. Demirdzic, Z. Lilek, and M. Peric, A Collocated Finite Volume Method for Predicting Flows At all Speeds, *Int. J. Numer. Meth. Fluids*, vol. 16, pp. 1029–1050, 1993.
46. T. E. Tezduyar, M. Senga, and D. Vicker, Computation of Inviscid Supersonic Flows around Cylinders and Spheres with the SUPG Formulation and YZβ Shock-Capturing, *Comput. Mech.*, vol. 38, pp. 469–481, 2006.
47. F. Rispoli, R. Saavedra, F. Menichini, and T. E. Tezduyar, Computation of Inviscid Supersonic Flows around Cylinders and Spheres with the V-SGS Stabilization and YZβ Shock Capturing, *ASME J. Appl. Mech.*, vol. 76, no. 2, 020601, doi: 10.1115/1.3062969, 2009.
48. N. A. Modesto-Madera, A Numerical Study of Supersonic Flow past a Circular Cylinder, A Finite Volume Implementation, Master of Engineering Thesis, Rensselaer Polytechnic Institute, Hartford, CT, 2010.
49. A. H. Shapiro, *The Dynamics and Thermodynamics of Compressible Fluid Flow*, John Wiley & Sons, Inc., 1953.
50. A. M. Blokhin and D. L. Tkachev, Stability of a Supersonic Flow about a Wedge with Weak Shock Wave, *Sbornick: Mathematics*, vol. 200, no. 2, pp. 157–184, 2009.
51. M. S. Khalid and A. M. Malik, Modeling and Simulation of Supersonic Flow Using McCormack's Technique, in *Proceedings of the World Congress on Engineering 2009 Vol II, WCE 2009*, July 1–3, London, U.K., 2009.
52. V. Elling and T. -P. Liu, Supersonic Flow onto a Solid Wedge, *Commun. Pure Appl. Math.*, vol. 61, pp. 1347–1448, 2008.
53. M. J. Grismer, Numerical Simulations of Steady and Unsteady Oblique Detonation Phenomena with Application to Propulsion, Ph.D. thesis, Department of Aerospace and Mechanical Engineering, Notre Dame university, Notre Dame, In, 1994.
54. J. D. Anderson, *Modern Compressible Flow with Historical Perspective*, McGraw-Hill, New York, 1982.
55. www.grc.nasa.gov/WWW/k-12/airplane/wdgflow.html.
56. F. S. Lien and M.A. Leschziner, A Pressure-Velocity Solution Strategy for Compressible Flow and Its Application to Shock-Boundary-Layer Interaction Using Second-Moment Turbulence Closure, *J. Fluids Eng.*, vol. 115, pp. 717–725, 1993.